# Modelling of bifacial photovoltaic farms to evaluate the profitability of East/West vertical configuration

Baricchio, M.; Korevaar, Marc; Babal, Pavel; Ziar, Hesan

**DOI**
10.1016/j.solener.2024.112457

**Publication date**
2024

**Document Version**
Final published version

**Published in**
Solar Energy

**Citation (APA)**
Baricchio, M., Korevaar, M., Babal, P., & Ziar, H. (2024). Modelling of bifacial photovoltaic farms to evaluate the profitability of East/West vertical configuration. *Solar Energy*, *272*, Article 112457. https://doi.org/10.1016/j.solener.2024.112457

Solar Energy 272 (2024) 112457

Contents lists available at ScienceDirect

Solar Energy

journal homepage: www.elsevier.com/locate/solener

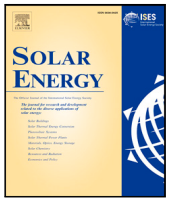

# Modelling of bifacial photovoltaic farms to evaluate the profitability of East/West vertical configuration

Matteo Baricchio [a,*], Marc Korevaar [b], Pavel Babal [b], Hesan Ziar [c]

[a] DCSC Group, Delft University of Technology, Delft, The Netherlands
[b] Kipp&Zonen, Delft, The Netherlands
[c] PVMD Group, Delft University of Technology, Delft, The Netherlands

ARTICLE INFO

*Keywords:*
Bifacial PV modules
PV modelling
View factor
Solar electricity market
Vertical modules

ABSTRACT

East/West (E/W) vertical bifacial photovoltaic (PV) modules can achieve higher profits than the conventional North/South (N/S) tilted configuration depending on the design choices and external conditions. In this study a model based on 2D view factor concept is developed to estimate the power generated by a large-scale bifacial PV farm, considering the non-uniformity of the incident irradiance and the spectral impact. A validation using measured data is performed, focusing on the non-uniformity of the rear irradiance. This model is used to compare the profitability between E/W vertical and N/S tilted PV farm configurations, considering higher prices during noon with respect to morning/evening periods. The results identify the ratio between these two price values as the key variable that influences the comparison between the PV farm configurations. Specifically, a sufficiently high price ratio ensures the higher profitability of E/W vertical modules, however, the exact value is dependent on the location and the design variables. In general, higher row-to-row distance and lower diffuse fraction enhance the profitability of the E/W vertical over the N/S tilted configuration. On the other hand, elevation of the modules, curtailment strategies and hybrid solutions have a minor influence.

## 1. Introduction

Solar photovoltaic (PV) has seen the most rapid growth in the period from 2010 to 2022 among the renewable energy sources, reaching a global cumulative installed capacity of 1047 GW at the end of 2022 [1]. Currently, bifacial PV modules represents 30% of the market share, but this value will rise up to 70% in the next 10 years according to the estimations [2]. The peculiarity of bifacial PV modules consists of their property of absorbing the irradiance on both sides of the PV module. This can lead to an increase in the generated power up to 30% [3], which increases the energy density of such technology in comparison with monofacial case. However, this gain in performance is highly dependent on the ground type, whose reflecting properties determine the amount of light incident on the rear surface of the modules [4]. On the other hand, the extra energy provided by the bifacial solar cells involves some additional investment costs. In the recent years, a significant decrease in these costs has made bifacial PV a competitive option in terms of levelized cost of electricity worldwide [5].

Models that are able to predict the power generated by bifacial PV modules are required to determine the potential and the applicability of this technology. These can be divided into optical and thermo-electrical sub-models. The latter sub-model relies on conventional concepts, widely adopted for monofacial PV modelling. In contrast, the former sub-model adds complexity due to the presence of rear irradiance, resulting from multiple reflections and generating a non-uniform incident profile. In the recent years, different optical models have been developed to estimate the irradiance incident on bifacial PV modules. Various approaches have been explored for this purpose and they can be divided into two categories, depending whether they are based on the concept of view factor or ray-tracing [6]. Inherited by heat transfer theory, view factor method is widely adopted in the literature due to the low computational time [7] and it is based on the assumption of isotropic scattering of the reflected rays [8]. Conversely, ray-tracing software packages such as RADIANCE [9] are based on individual sunrays simulations, increasing the accuracy of the results as well as the simulation time [7]. Irrespective of the approach, there are other aspects that can be integrated into the models such as non-uniformity of the rear irradiance [10], spectral impact of the incident radiation [11] and influence of the mounting structure [12]. However, the integration of these aspects into current models is often limited when the main purpose of the studies is to enable fast simulations over multiple locations and extended time periods.

* Corresponding author.
*E-mail address:* m.baricchio@tudelft.nl (M. Baricchio).

https://doi.org/10.1016/j.solener.2024.112457
Received 9 January 2024; Received in revised form 15 February 2024; Accepted 10 March 2024
Available online 18 March 2024

**Nomenclature**

| | |
|---|---|
| $\gamma$ | Limit of the angular sector for cell/ground view factor |
| $\lambda$ | Wavelength |
| $\phi_{Bi}$ | Bifaciality factor |
| $\rho$ | Albedo |
| $\theta$ | Tilt angle |
| $\theta_{opt}$ | Optimal tilt angle |
| $a_g$ | Ground direct component fraction factor |
| $A_m$ | Module's orientation |
| $A_s$ | Sun's azimuth |
| $a_s$ | Sun's altitude |
| $a_{s,max}$ | Maximum sun's altitude of the price curve |
| $a_{s,min}$ | Minimum sun's altitude of the price curve |
| $a_{sky}$ | Sky direct component fraction factor |
| $AOI$ | Angle of incidence with respect to normal direction |
| $AOI_{2d}$ | Angle of incidence in the plane of interest |
| $AOI_g$ | Angle of incidence for ground segment |
| $BG$ | Bifaciality gain |
| $c$ | Length of the cell |
| $c_{ff}$ | Fill factor coefficient |
| $c_{light}$ | Speed of light in vacuum |
| $d$ | Row-to-row distance |
| $DHI$ | Diffuse horizontal irradiance |
| $DNI$ | Direct normal irradiance |
| $e$ | Electricity price |
| $EQE_{front}$ | External quantum efficiency of the front cell |
| $EQE_{rear}$ | External quantum efficiency of the rear cell |
| $EY$ | Energy yield |
| $f_{AOI,dif}$ | AOI correction factor for diffuse irradiance |
| $f_{AOI,dir}$ | AOI correction factor for direct irradiance |
| $f_{AOI,g}$ | AOI correction factor for ground irradiance |
| $f_{AOI,m}$ | AOI correction factor for module-reflected irradiance |
| $f_{shape}$ | Shape factor of the price curve |
| $FF$ | Fill factor |
| $G_{front}$ | Front broadband irradiance |
| $G_{NOCT}$ | NOCT irradiance at STC |
| $G_{rear}$ | Rear broadband irradiance |
| $G_{STC}$ | Broadband irradiance at STC |
| $G_{tot}$ | Total broadband irradiance |
| $GHI$ | Global horizontal irradiance |
| $GNU$ | Non-uniformity of rear irradiance |
| $h$ | Module's elevation |
| $h$ | Planck constant |
| $h_{opt}$ | Optimal module's elevation |
| $I_{dif,circ}$ | Circumsolar diffuse irradiance |
| $I_{dif,hor}$ | Horizon diffuse irradiance |
| $I_{dif,iso}$ | Isotropic diffuse irradiance |
| $I_{front}$ | Total irradiance incident on cell's front side |
| $I_{ground}$ | Ground-reflected irradiance |
| $I_{mod}$ | Irradiance reflected by the neighbouring modules |
| $I_{neigh}$ | Average irradiance incident on neighbouring modules |
| $I_{rear}$ | Total irradiance incident on cell's front side |
| $I_{sc,STC}$ | Short-circuit current of the module at STC |
| $I_{sky}$ | Sky irradiance |
| $J_{sc,front}$ | Short-circuit current density of cell's the front side |
| $J_{sc,rear}$ | Short-circuit current density of cell's rear side |
| $J_{sc}$ | Short-circuit current density |
| $k$ | Boltzmann constant |
| $k_{J_{sc}}$ | Current temperature coefficient |
| $k_{V_{oc}}$ | Voltage temperature coefficient |
| $l$ | Length of the module |
| $LCOE$ | Levelized cost of electricity |
| $MM_{loss}$ | Mismatch losses |
| $n$ | Ideality factor |
| $N_p$ | Number of strings connected in parallel in a module |
| $N_s$ | Number of cells connected in series in a module |
| $n_{max,power}$ | Maximum power fraction in case of curtailment |
| $n_{vert}$ | Ratio vertical/total modules in a hybrid farm |
| $p$ | Atmospheric pressure |
| $p_{max}$ | Maximum price of the price curve |
| $p_{min}$ | Minimum price of the price curve |
| $P_{module}$ | Power generated by a module |
| $P_{rated}$ | Rated power |
| $p_{ratio}$ | Price ratio of the price curve |
| $q$ | Elementary charge |
| $R$ | Revenues |
| $r$ | Reflectivity of the module |
| $R_{gain}$ | Revenues gain |
| $SVF$ | Sky view factor |
| $SVF_g$ | Ground sky view factor |
| $T_{amb}$ | Ambient temperature |
| $T_{cell}$ | Temperature of the cell |
| $T_{INOCT}$ | INOCT temperature of the module |
| $T_{NOCT}$ | NOCT temperature of the module |
| $V_{oc,STC}$ | Open-circuit voltage of the module at STC |
| $V_{oc}$ | Open-circuit voltage |
| $v_{oc}$ | Adimensional voltage |
| $VF_{c\to g}$ | View factor between cell and ground segment |
| $VF_{c\to m}$ | View factor between cell and neighbouring module |
| $w$ | Width of the module |

Models are often adopted to simulate the performance of large bifacial PV farms, optimizing design parameters such as tilt, orientation, elevation, and row-to-row distance. Various studies explore different configurations, including vertically-mounted systems [5,13,14]. Vertical modules are installed in the East/West (E/W) orientation to exploit morning and evening sun irradiation, exhibiting a two-peak power curve with a minimum at noon, unlike conventional North/South (N/S) orientation of tilted modules that leads to a maximum in power production around noon [3]. Despite the generally lower energy yield of the E/W vertical configuration compared to the N/S tilted counterpart, this arrangement offers two main advantages

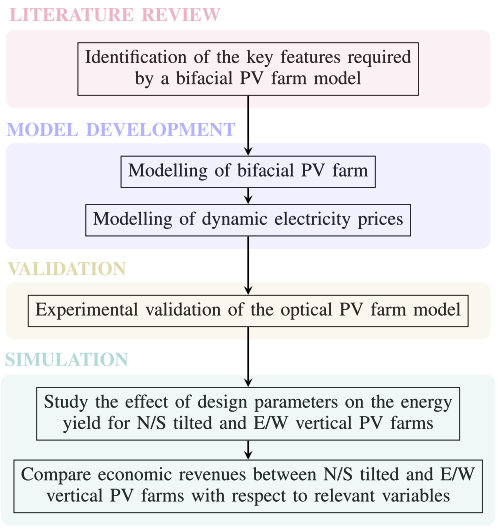


**Fig. 1.** Outline of the research.

that increase its appeal in the market. First, the physical mounting structure allows for versatile integration of the modules in various applications, such as agrivoltaics [15–25] and noise barriers [26–28], while reducing the soiling losses [29]. Second, the shape of the power curve provides several benefits, including improved demand-supply matching [30,31], reduced storage capacity requirements [32,33], and mitigation of the duck-curve problem [34]. Additionally, the similarity between the generated daily power profile and electricity day-ahead market prices can lead to increased revenues [19]. Specifically, a two-peak power curve is favoured by scenarios where a substantial price gap between morning/evening and noon prices is present, as observed when solar energy constitutes a significant portion of a country's electricity mix [35]. Nonetheless, the literature lacks of a complete study that analyzes the profitability of the vertical modules with respect to the conventional configuration according to the authors' knowledge.

The contribution of this work is twofold. First, a model is developed to estimate the power generated by a bifacial PV farm, enabling large scale simulations without neglecting key aspects such as non-uniformity of the rear irradiance and spectral impact. Second, this study quantifies the profitability of the E/W vertical bifacial PV farm configuration with respect to the N/S tilted counterpart.

This paper is structured as follows. In Section 2 an overview of the models adopted in previous studies to simulate the operation of bifacial modules is outlined. The opto-thermo-electrical and the electricity market models developed for this analysis are explained in Sections 3 and 4, respectively. Subsequently, Section 5 describes the experimental validation of the optical model. Lastly, the results are discussed in Section 6 whereas the conclusions are included in Section 7. Fig. 1 summarizes the structure of the paper, containing the outline of the research.

## 2. Literature review on bifacial PV models

### 2.1. Metrics of bifacial PV

The comparison between different bifacial PV installations is based on various metrics that consider diverse aspects of this technology and its operation. The bifaciality property of the solar cells is assessed using the bifaciality factor ($\phi_{Bi}$), namely the ratio between the power generated by the rear side and by the front side under standard test conditions (STC). The values usually range from 60% to 90% in commercial applications [8] whereas $\phi_{Bi}$ up to 92% and 95% are reported for Silicon Heterojunction and n-PERT solar cells, respectively [36]. The surplus of energy generated by bifacial modules with respect to the monofacial is quantified by the bifacial gain ($BG$), which depends on the location as well as the design parameters. Such aspects influence also the levelized cost of electricity ($LCOE$), adopted to compare the cost-effectiveness of different PV technologies [13]. In relation to the electricity market, the value factor quantifies the ability to capture higher electricity prices by a power plant, determining the benefits of the daily power curve shape of various configurations [37].

### 2.2. View factor vs. ray-tracing

The view factor concept is adopted to estimate the radiation incident on different surfaces and is defined as shown in Eq. (1) [38]. In this definition, the view factor between two surfaces, denoted by $A_1$ and $A_2$, is formulated by $\theta_1$, $\theta_2$ and $s$ as the angles with respect to the normal directions of the two surfaces and their distance, respectively. The analytical solution of the integral included in Eq. (1) can be obtained only for limited cases hence numerical methods or approximations are utilized, including Nusselt unit spheres approach [39], Monte Carlo simulations [40] and Hottel's cross string rule [41,42]. This last method is based on a 2D approximation and it is widely adopted in the field of PV modelling due to its low computational time achieved by neglecting the edge effects [8], i.e. the increase of the irradiance received by the modules at the edge of the row due to the presence of less obstacles. However, the impact of the approximation is limited in case of large-scale PV farms, for which the infinite rows' assumption leads to minimal errors.

$$F_{A_1 \to A_2} = \frac{1}{A_1} \iint_{A_1 A_2} \frac{\cos\theta_1 \cos\theta_2}{\pi s^2} dA_1 \, dA_2 \tag{1}$$

Ray-tracing consists of the simulation of individual rays' path to obtain an illumination mapping through a rendering process. RADIANCE [9] is a widely used open-source software adopted for PV modelling purposes [43] and NREL recently released the version bifacial_radiance [44] specifically for bifacial PV applications. It enables the modelling of 3D complex environments, capturing the edge effects, the influence of the racking system and the non-uniformity on the spatial dimension [45], increasing the accuracy in comparison to view factor techniques. However, such method requires a computational time up to $10^4 - 10^5$ higher with respect to 2D view factor methods [45].

### 2.3. Non-uniformity of the rear irradiance

One of the main drawbacks in bifacial PV technology is the non-uniformity of the irradiance incident on the rear side of the module, which causes mismatch losses ($MM_{loss}$) up to 1.5% on the annual energy yield [46]. Such non-uniformity arises from multiple causes, e.g. inconstant field of view of PV cells to the different elements, alternating shaded/unshaded patterns, presence of the mounting structure, and heterogeneity of the ground. Various metrics have been proposed to quantify its magnitude, including $GNU$, defined as shown in Eq. (2) [47]. $G_{max}$ and $G_{min}$ refer to the maximum and the minimum irradiance incident on the front or rear surface of a PV module.

$$GNU = \frac{G_{max} - G_{min}}{G_{max} + G_{min}} \tag{2}$$

To take into account the effect of the non-uniformity, the spatial resolution of the irradiance is often increased from module to cell level in multiple studies. Alternatively, empirical relations to estimate $MM_{loss}$ have been developed by Raina and Sinha [10] based on $GNU$ obtaining $R^2 = 98.1\%$ whereas an accuracy up to $R^2 = 0.995$ is achieved by Deline et al. [46], considering the mean standard deviation and the mean absolute difference of rear irradiance distribution.

### 2.4. Spectral influence

Solar cells are spectrally-sensitive devices, hence the power generated is dependent on the spectrum of the incoming radiation. The spectrum of ground-reflected irradiance, dominant among the rear side components, is dependent on the specific ground type, increasing the complexity of spectral impact in case of bifacial modules [11]. Therefore, several studies recommend to consider the spectral effect while developing bifacial PV models [11,48–50] since the use of a constant scalar albedo could lead to relative errors in bifacial gain calculations up to 19.5% [50]. Even though the spectral impact is often neglected in the existing bifacial models, different approaches have been developed to tackle this issue, ranging from using spectral data to including corrective coefficients [13].

### 2.5. Classification of optical models

Aiming to select the proper model's features for the objective of this research, the optical bifacial models utilized in 47 different studies spanning from year 2013 to 2022 have been reviewed. Fig. 2 maps the existing literature based on three key features, namely spectral impact, non-uniformity of the rear irradiance and geographical scale, with a distinction between view factor and ray tracing approaches.

### 2.6. Thermo-electrical models

Depending on the requirements in terms of accuracy and computational resources, various models are adopted to estimate the cells' temperature. These include INOCT [51], Sandia [52], Faiman [53], Janssen [54] models or other alternatives which require a large number of input parameters and/or intensive computational resources, e.g. fluid-dynamics model [55]. The same requirements determine the electrical sub-model, which range from constant efficiency expressions [13] to 2-diode model approximation [56].

### 2.7. Characteristics of the model developed in this study

Considering the objective of this study, a low computational time represents the main requirement due to the target global scale analysis, hence a 2D view factor approach is selected despite its lower accuracy. Furthermore, Fig. 2 highlights that the existing literature lacks a model capable of effectively considering both the non-uniformity of the rear irradiance and the spectral influence across a large number of locations. This study endeavors to bridge this gap by introducing a multi-dimensional matrix approach. For this reason, the software MATLAB is used to implement the models and perform the simulations discussed in this paper.

## 3. Bifacial PV farm model

### 3.1. Structure of the optical sub-model

The optical sub-model calculates the irradiance incident on the bifacial PV modules and is based on view factor concept while adopting the 2D "large-farm" assumption, which entails infinite row length. The non-uniformity of the irradiance and the spectral impact are considered by using a four-dimensional matrix as the base unit to perform annual farm simulation. The first and the second dimensions represent spatial irradiance distributions along farm rows and modules' cells, respectively, whereas the third and fourth refer to the time and sunlight wavelength. Therefore, high computational performance is achieved by replacing prolonged iterations with matrices operations. However, this increases the complexity of the algorithm, involving matrices up to the sixth dimension and continuous decoupling of sub-problems to avoid excessive computational heaviness. Additionally, the matrix structure allows to assign different design parameters for each row, enabling to test unconventional configurations. In summary, using this method the irradiance is calculated for every wavelength of the spectrum on cell level while conserving the computational time. The total irradiance incident on front and rear solar cells is determined by three different components, discussed in the next subsections: (i) Sky irradiance ($I_{sky}$), (ii) Ground-reflected irradiance ($I_{ground}$), (iii) Irradiance reflected by neighbouring modules ($I_{mod}$).

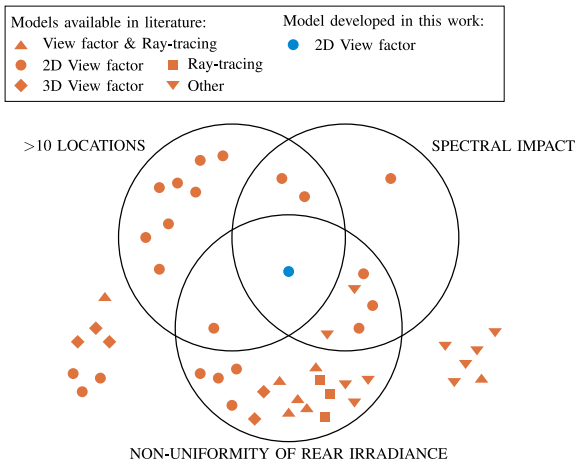


**Fig. 2.** Venn diagram of the bifacial PV models available in literature [5,7,8,10,11,13,26,36,43,46–49,54,57–89].

### 3.2. Irradiance decomposition

Perez Sky Diffuse model [90] is used to decompose the $DHI$ into circumsolar ($I_{dif,circ}$), isotropic ($I_{dif,iso}$) and horizon ($I_{dif,hor}$) diffuse components. These are used to estimate the direct and diffuse contribution of the irradiance incident on the PV cells.

### 3.3. Ground segmentation

The pattern created by the shadows projected by the modules on the ground is calculated, obtaining a series of unshaded and shaded segments that depend on the sun's position and the design parameters. To estimate the irradiance incident on the ground, its sky view factor has to be calculated, which is a spatially continuous function hence requiring a fine ground segmentation. Therefore, the ground sky view factor ($SVF_g$) is calculated for each ground segment, whose length influences the accuracy of the model. The calculation of $SVF_g$ is limited to the angular sectors between the nearest four rows to each segments, identified by $\gamma_{2i-1}$ and $\gamma_{2i}$, as shown in Eq. (3) and Fig. 3(a).

$$SVF_g = \sum_{i=1}^{3} \frac{\cos(\gamma_{2i-1}) - \cos(\gamma_{2i})}{2} \tag{3}$$

whereas $SVF_g$ determines the amount of diffuse irradiance reaching a ground segment, $a_g$ quantifies the fraction of direct component and it is defined as follows, where $AOI_g$ indicates the angle of incidence.

$$a_g = \begin{cases} 0 & \text{if segment is shaded} \\ \max\left(0, \cos(AOI_g)\right) & \text{if segment is unshaded} \end{cases} \tag{4}$$

### 3.4. Field of view

To calculate the influence of each of the surrounding elements, the field of view of each solar cell is determined, namely the 180° view is divided into angular sectors associated to sky, ground and neighbouring modules. This is implemented for both front and rear cells and an example for the latter case is depicted in Fig. 3(d).

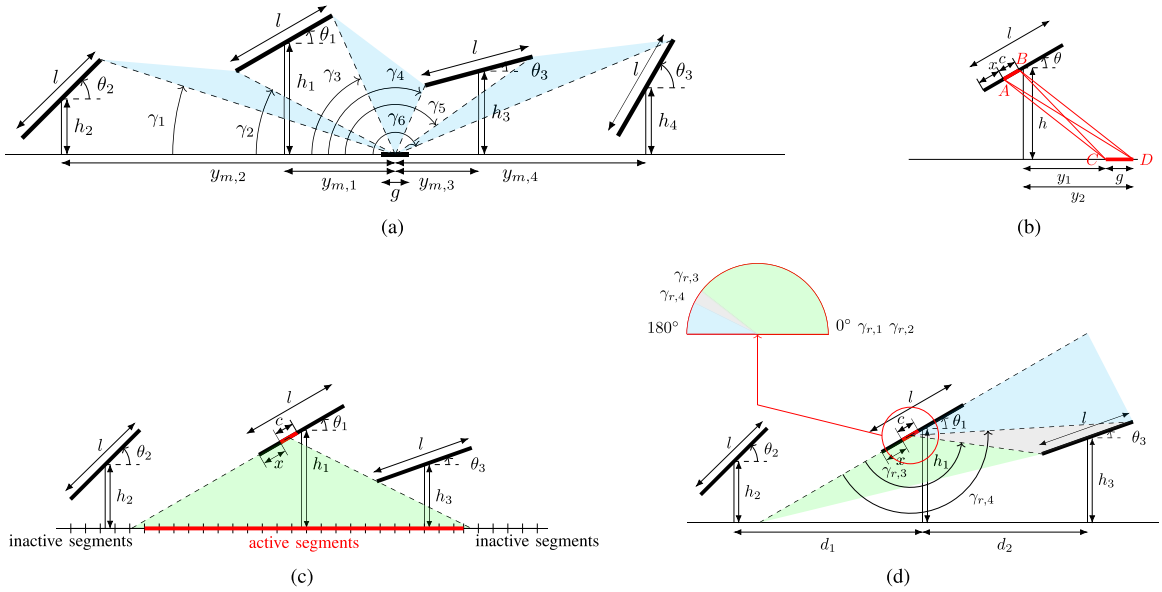


**Fig. 3.** Working principle of the optical model: (a) Sky view factor of a ground segment, (b) View factor between a cell and a ground's segment, (c) active segments for a rear cell, (d) field of view of a rear cell.

### 3.5. Sky irradiance

The sky irradiance is calculated according to Eq. (5), where both direct and diffuse contributions are included.

$$I_{sky} = a_{\text{sky}} \cdot f_{AOI,dir} \cdot (DNI + I_{dif,circ}) + SVF \cdot f_{AOI,dif} \cdot I_{dif,iso} \tag{5}$$

Only unshaded cells receive direct irradiance and such condition is satisfied when the 2D projection of the sunrays angle of incidence ($AOI_{2d}$) on the plane of interest is within the sky sector identified in the field of view of the specific cell. The shaded/unshaded condition is included through the factor $a_{sky}$, defined in Eq. (6), where $AOI$ indicates the angle of incidence with respect to the cells' normal direction.

$$a_{sky} = \begin{cases} \cos(AOI) & \text{if the cell is unshaded} \\ 0 & \text{if the cell is shaded} \end{cases} \tag{6}$$

Diffuse sky component depends on the sky view factor ($SVF$), which is calculated as shown in Eq. (7), where $\gamma_{sky_1}$ and $\gamma_{sky,2}$ define the sky angular sector identified in the field of view.

$$SVF = \frac{\cos(\gamma_{sky,1}) - \cos(\gamma_{sky,2})}{2} \tag{7}$$

Lastly, $f_{AOI,dir}$ and $f_{AOI,dif}$ are the $AOI$ correction factors based on the model of Martin and Ruiz [91]. Whereas the former is determined by the $AOI$, for the latter the average between the values of a one-degree-resolution series of angles within the extremes of the angular sector is adopted.

### 3.6. Ground-reflected irradiance

The contribution to the ground-reflected irradiance is limited to segments seen by a cell, appointed as "active" in this study, as highlighted in Fig. 3(c). This status depends on the field of view, i.e. segments are considered active when they are entirely enclosed in the projection of the ground angular sector. The ground-reflected irradiance is calculated according to Eq. (8). $f_{AOI,g}$ is the $AOI$ correction factor determined similarly to the sky direct component whereas $\rho$ indicates the albedo, for which both scalar and spectral values are supported. Lastly, Eq. (9) adopted for the view factor between a solar cell and a ground segment ($VF_{c\to g}$) is based on Hottel's cross string rule, where the nomenclature refers to Fig. 3(b).

$$I_{ground} = \rho \cdot \sum_{\substack{\text{active} \\ \text{segments}}} f_{AOI,g} \cdot VF_{c\to g} \cdot \left(a_g \cdot (DNI + I_{dif,circ}) + SVF_g \cdot I_{dif,iso}\right) \tag{8}$$

$$VF_{c\to g} = \frac{BC - AC + AD - BD}{2 \cdot c} \tag{9}$$

### 3.7. Irradiance reflected by neighbouring modules

The irradiance component consisting of neighbouring modules reflections is calculated through Eq. (10). This is proportional to the irradiance incident on such modules, wherein an average spatial value is considered ($I_{neigh}$). $VF_{c\to m}$ is the view factor between the cell and the neighbouring module, based on the field of view, similarly to $VF_{c\to g}$. $r$ indicates the reflectivity of the modules whereas $f_{AOI,m}$ is computed analogously to the sky diffuse irradiance.

$$I_{mod} = r \cdot VF_{c\to m} \cdot f_{AOI,m} \cdot I_{neigh} \tag{10}$$

### 3.8. Thermo-electrical sub-model

The choice of the thermal model to predict cells temperature ($T_{cell}$) is based on two criteria, namely the availability of data for the analysed locations and the computational time restrictions. These reasons lead to adopt the INOCT model [51] to estimate the temperature of the modules, considering a rack mounted system. Concerning the electrical model, preliminary tests adopting 1-diode approximation have failed the computational time requirements due to the global-scale of the analysis hence a fill factor ($FF$) approximation introduced by Green [92] is adopted. Eqs. (11)–(14) [56] are implemented to estimate the short-circuit current density ($J_{sc}$) and the open-circuit voltage ($V_{oc}$) of every cell, where front and rear sides are modelled as parallel circuits. Specifically, two different EQE curves are adopted to distinguish front and rear cells, namely $EQE_{front}(\lambda)$ and $EQE_{rear}(\lambda)$.

$$J_{sc,front} = \frac{q}{h\, c_{light}} \cdot \left(1 + k_{J_{sc}} \cdot (T_{cell} - 25\ ^\circ\text{C})\right) \cdot \int_{\lambda_1}^{\lambda_2} I_{front}(\lambda) \cdot EQE_{front}(\lambda)\, d\lambda \tag{11}$$

$$J_{sc,rear} = \frac{q}{h\,c_{light}} \cdot \left(1 + k_{J_{sc}} \cdot (T_{cell} - 25\ °\mathrm{C})\right) \cdot \int_{\lambda_1}^{\lambda_2} I_{rear}(\lambda) \cdot EQE_{rear}(\lambda)\, d\lambda \tag{12}$$

$$J_{sc} = J_{sc,front} + J_{sc,rear} \tag{13}$$

$$V_{oc} = \left[\frac{V_{oc,STC}}{N_s} + \frac{nk \cdot (T_{cell} + 273\ \mathrm{K})}{q} \cdot \log\left(\frac{G_{tot}}{G_{STC}}\right)\right] \cdot \left(1 + k_{V_{oc}} \cdot (T_{cell} - 25\ °\mathrm{C})\right) \tag{14}$$

Green approximation is based on the relations (15) and (16) [92], where the constant $c_{ff}$ is tuned by minimizing the error with respect to the 1-diode model. For this study, this value is set equal to 200, limiting the error in the annual energy yield up to 0.7%. The relatively high magnitude is caused by the neglect of the cells' interconnection losses and the logarithmic nature of the relation.

$$FF = \frac{v_{oc} - \log\left(v_{oc} + c_{ff}\right)}{v_{oc} + 1} \tag{15}$$

$$v_{oc} = \frac{qV_{oc}}{k(T_{cell} + 273\ \mathrm{K})} \tag{16}$$

The symbols present in the Eqs. (11)–(16) are defined as follows. $I_{front}(\lambda)$ and $I_{rear}(\lambda)$ are the spectral irradiance values incident on the front and the rear side, integrated between the wavelengths $\lambda_1$ and $\lambda_2$. The constants $q, h, c_{light}, k$ are the elementary charge, the Planck's constant, the speed of light in vacuum and the Boltzmann constant, respectively. $k_{J_{sc}}$ and $k_{V_{oc}}$ indicate the current and the voltage temperature coefficients whereas $N_s$ is the number of cells connected in series. $V_{oc,STC}$ is the module's open-circuit voltage at Standard Test Conditions. $n$ is the ideality factor, $G_{STC}$ is the broadband irradiance at STC and $G_{tot}$ is the total integrated irradiance.

Lastly, the total power generated by a PV module is obtained according to Eq. (17), where for every cell the open circuit voltage ($V_{oc,i}$), the fill factor ($FF_i$) and the area ($A_{cell}$) are multiplied to the minimum current density ($J_{sc,i}$) generated within a string. Moreover, the effect of bypass diodes is considered by choosing the configuration that maximizes the power, i.e. excluding from Eq. (17) the string that generates less current. Once the power of each module is computed, the values are summed to obtain the total power of the farm and integrated over the time period to calculate the energy yield.

$$P_{module} = \left(\sum_{i=1}^{N_{cell}} V_{oc,i} \cdot FF_i \cdot A_{cell}\right) \cdot \min_{i \in N_{cell}} J_{sc,i} \tag{17}$$

## 4. Electricity market model

Analysing a few selected European countries, a negative correlation between electricity prices and sun's altitude ($a_s$) is observed, i.e. price values are minimal during noon. Moreover, an increase (in absolute value) of the correlation has been registered in 2022 with respect to 2018 [35], proving the sensitivity on the PV installed capacity. This is illustrated in Fig. 4. To enable the simulation of different market scenarios, electricity prices are modelled depending on $a_s$, creating an annual price curve for each location. Specifically, five different parameters are used to determine the shape of the price timeseries: (i) price ratio ($p_{ratio}$), (ii) minimum price ($p_{min}$), (iii) minimum sun's altitude ($a_{s,min}$), (iv) maximum sun's altitude ($a_{s,max}$), and (v) shape factor ($f_{shape}$). The resolution of the price curve depends on the $a_s$ input array and the price values oscillate between the minimum "noon price" ($p_{min}$) and the maximum "morning/evening price" calculated as $p_{min} \cdot p_{ratio}$. The transition between these prices is defined by $a_{s,min}$, $a_{s,max}$ and $f_{shape}$. Specifically, $a_s$ values that satisfy the condition $a_s < a_{s,min}$ are associated with the maximum price whereas the minimum price

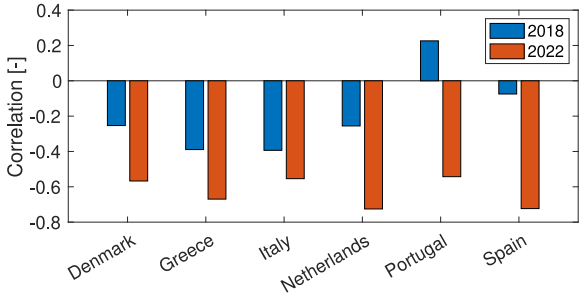


**Fig. 4.** Correlation between electricity prices and $a_s$ of few selected countries in Europe.

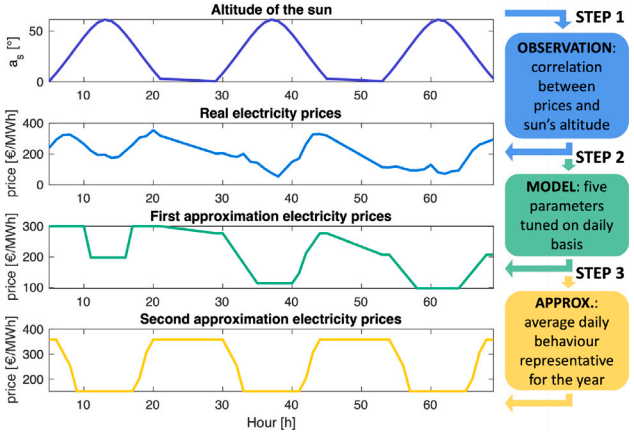


**Fig. 5.** Main steps in the modelling of the electricity prices. This example refers to the period 16–18 June 2022 of the Netherlands.

is assigned to $a_s$ values such that $a_s > a_{s,max}$. Lastly, $f_{shape}$ is an integer number that determines the presence of intermediate prices between the maximum and the minimum values since it is defined as the number of possible values that can be assumed by the price curve, e.g. $f_{shape} = 2$ leads to a rectangular curve. Moreover, a seasonal effect is intrinsic in this method due to the $a_s$ dependence, e.g. higher prices are obtained during the winter period due to lower average $a_s$ values in the Northern hemisphere. These five parameters are tuned using real electricity prices of 8 European countries registered between 2018 and 2022, i.e. 16 cases in total. Minimizing RMSE on daily basis, 365 values of $p_{ratio}$, $p_{min}$, $a_{s,min}$, $a_{s,max}$ and $f_{shape}$ are found for each case. Definitive values are obtained through two averaging processes. First, for each specific case yearly average values are assumed to be representative for the entire year. Second, average values among the 16 different cases are calculated to generalize the results on a global scale. Whereas different values of $p_{ratio}$ and $p_{min}$ are tested to simulate various market conditions, $a_{s,min}$, $a_{s,max}$ and $f_{shape}$ are kept constant during this study and their values are 5.4°, 32.5° and 4, respectively. The process of electricity prices modelling is summarized in Fig. 5.

## 5. Experimental work for model validation

The validation of the model is limited to the estimation of the rear irradiance incident on different positions along the modules length. The other sub-models have been widely validated in the recent years due to the use for monofacial modules [7]. This validation has been conducted in collaboration with the company *Kipp & Zonen* which has performed a series of measurements using their setup and sensors. The measurements took place in Delft (52.0°N, 4.4°E) between July and September 2020. The experimental setup comprehends three bifacial PV modules equipped with six pyranometers on the rear side, as depicted in Fig. 6.

**Fig. 6.** Experimental setup provided by the company *Kipp & Zonen*.

Additional structures and monofacial modules have been placed next to the bifacial modules to simulate the farm environment. Data gathered during 12 different days have been selected for this analysis and both the tilt and the ground type were varied to test the performance of the model under diverse installation conditions. Front irradiance has been measured as well in order to quantify the impact of the rear component deviations on the total value. A 15-min resolution is adopted to mitigate the slight time misalignment between the sensors hence a time-averaging process has been performed to match the time resolution of the different signals, in accordance to the approach of Marion et al. [7]. Further information concerning the experimental setup are included in Appendix B.

## 6. Results and discussion

### 6.1. Results of the experimental validation

Modelled and measured data are compared by calculating the root mean square error (RMSE) and the mean bias deviation (MBD), which amount to 12.65 W/m$^2$ (21.69%) and −1.29 W/m$^2$ (−2.22%), respectively. These values refer to the overall comparison and are in the same range of the findings from previous studies based on view factor models [7]. Moreover, the validation has shown that the model offers a high accuracy when the combined front and rear irradiance is of interest while predicting only the rear component is more challenging. This can be observed in Fig. 7, where the left figure refers to the total incident irradiance wheres on the right only the rear component is considered. Additional results are included in the Appendix B.

Further analysis is performed to investigate the conditions and the parameters that mostly affect the model's ability to predict the incident irradiance, as highlighted in Fig. 8. A slight trend with respect to the hour of the day can be observed, where higher errors are obtained during morning and evening periods. Three different reasons have been identified as possible causes for this behaviour. First, the non-representativeness of the limited system's size with respect to a large PV farm leads to more evident consequences at lower solar angles. Second, the different light's transmission properties of the wooden panels present in the setup could affect more the rear irradiance during lower sun's altitudes. Third, partial shading and extra-reflections caused by the surrounding environment occur during morning and evening periods, influencing the measurements. On the other hand, an evident trend concerns the tilt values, i.e. high tilts lead to an overestimation of the irradiance whereas an underestimation is registered in case of low tilts. In general, it is observed that higher tilt values also cause larger errors on the estimation. Such behaviour can be explained by taking into account the limitations of the view factor approach, which assumes a diffuse reflection of the incident light. Therefore, the largest errors occur in case of higher tilts, for which a larger portion of unshaded ground is visible by the rear cells, hinting that the hypothesis of diffuse surfaces is inadequate for these ground segments. Such statement is also backed up by observing that larger errors occur at the edge of the modules, which have a wider view towards unshaded ground during clear sky conditions. Conversely, no clear trend is found with respect to the albedo, probably due to the lack of variety of measurements with respect to such feature. Lastly, the error in the estimation of $GNU$ is also investigated, resulting in underestimation of the non-uniformity for high tilt values and overestimation in case of low tilt values.

### 6.2. Input data

102 locations are selected for this study and their hourly data for a duration of one year are downloaded from the software Meteonorm [93]. These include broadband Direct Normal Irradiance ($DNI$) and Diffuse Horizontal Irradiance ($DHI$), sun's altitude ($a_s$) and azimuth ($A_s$), pressure ($p$) and ambient temperature ($T_{amb}$). Such variables allow the calculation of the Global Horizontal Irradiance ($GHI$) and the diffuse fraction, defined as the ratio between $DHI$ and $GHI$. These locations are highlighted in Fig. 9 along with the corresponding $GHI$-weighted average of diffuse fraction, assumed to be representative for the whole year. This is appointed as diffuse fraction in this analysis, unless otherwise specified. Spectral $DNI$ and $DHI$ curves are reconstructed from the broadband values using normalized irradiance-weighted average spectrum for both components [94], enabling the decoupling between spectral and temporal dimensions hence reducing the computational time. Light soil is adopted as ground type for the simulations, whose albedo spectral curve is obtained through the software SMARTS [95], assumed to be constant in time. Two different $EQE$ curves for the front and rear sides of the modules are taken from the work of Carolus et al. [96]. Therefore, $\phi_{Bi}$ is calculated as shown in Eq. (18) [36] and it is equal to 65.37% in this case. Detailed specifications of the modules considered in this work are included in Appendix C. Lastly, ground segments length is set to 0.2 m in order to limit the error to 0.15% on the annual energy yield caused by segments resolution.

$$\phi_{Bi} = \frac{J_{sc,rear}}{J_{sc,front}} = \frac{\int_{\lambda_1}^{\lambda_2} \frac{q}{hc} \cdot I_{STC}(\lambda) \cdot EQE_{rear}(\lambda)}{\int_{\lambda_1}^{\lambda_2} \frac{q}{hc} \cdot I_{STC}(\lambda) \cdot EQE_{front}(\lambda)} \tag{18}$$

### 6.3. PV farm configurations

As introduced in Section 1, the performance of two different farm configurations are compared in this study, namely N/S tilted and E/W vertical modules. Specifically, the tilt of the former configuration is chosen by maximizing the annual energy yield for each location and it is appointed as optimal tilt ($\theta_{opt}$). As expected, unlike monofacial PV modules, obtained $\theta_{opt}$ is highly sensitive on the installation conditions. In general, $\theta_{opt}$ is directly proportional to the row-to-row distance ($d$) whereas an opposite trend is obtained for the elevation of the modules ($h$). For simplicity, the optimal tilt values adopted for this study refer to the condition $d = 3$ m and $h = 1.5$ m because the impact of the design parameters decreases above these values.

### 6.4. Effect of design parameters on the energy yield

The impact of the design parameters differs depending on the farm configurations. This is observed by analysing the derivative of the energy yield with respect to row-to-row distance ($\frac{\partial EY}{\partial d}$) and modules height ($\frac{\partial EY}{\partial h}$), which are expressed as percentage of increase in the energy yield value for an increment of distance/height by 1 m.

Fig. 10 shows that $\frac{\partial EY}{\partial d}$ is always positive for both cases and the decreasing trend implies a saturation behaviour, i.e. an increase of $d$ leads to limited improvements in terms of energy yield after a certain limit. However, higher values of $\frac{\partial EY}{\partial d}$ are registered for the vertical configuration, meaning that $d$ has more impact in case a vertical PV farm is considered. Even though it cannot be detected from Fig. 10, such results are sensitive to $h$ as well, highlighting a strong

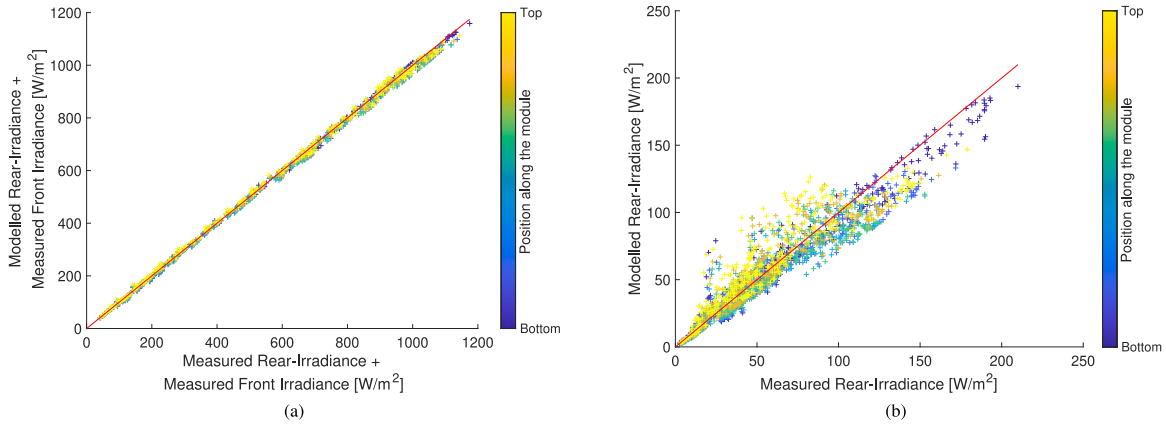


**Fig. 7.** Validation results: Comparison between modelled and measured data, considering both the total irradiance values, i.e. front+rear (a), and only the rear component (b).

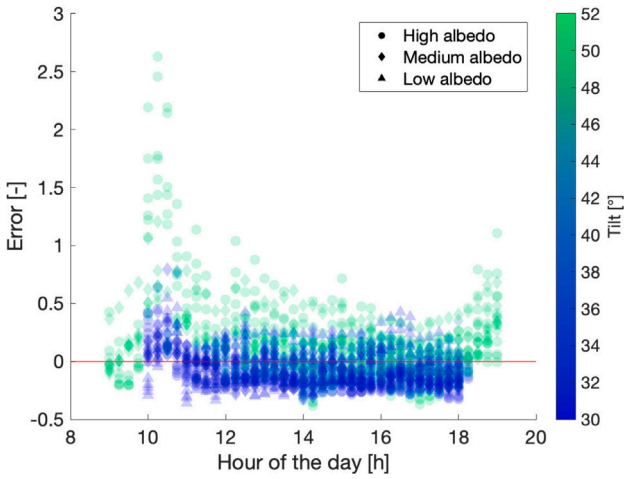


**Fig. 8.** Relative error on the rear irradiance estimation with respect to the hour of the day for different tilt and albedo values.

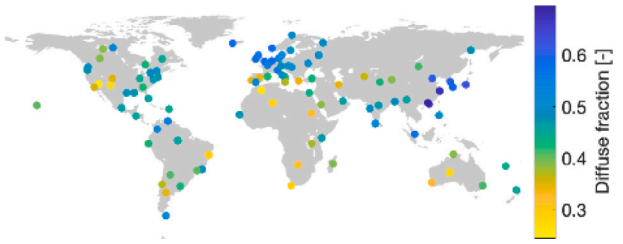


**Fig. 9.** Global map of the 102 locations analysed in this study. $GHI$-weighted average value of diffuse fraction is included for each location.

inter-dependence between these design parameters. Specifically, $\frac{\partial EY}{\partial d}$ is directly proportional to $h$ hence the benefits of larger $d$ values are greater in case of high module elevation. These general trends are valid for all the locations investigated in this study. However, the exact magnitude of the derivative is location dependent and no correlation with respect to the diffuse fraction is found.

$\frac{\partial EY}{\partial h}$ is analysed in Fig. 11, where a saturation behaviour similar to the previous case can be detected for both configurations. In contrast to the distance's influence, negative values of $\frac{\partial EY}{\partial h}$ are registered after a certain $h$ value in this case, highlighting the presence of an optimal height ($h_{opt}$) that maximizes the energy yield. Once such value is reached, a further increase in $h$ leads to minimal penalization in the energy yield hence the optimal height can be appointed as a saturation limit as well. Moreover, $h_{opt}$ depends not only on the farm configuration but also on the row-to-row distance and the specific location. In general, higher values of $h_{opt}$ are obtained for tilted modules with respect to the vertical counterpart. Moreover, in the tilted case $h_{opt}$ is proportional to $d$ value whereas such trend is not evident for vertical modules.

**Table 1**
Influence of $d$ and $h$: whether high, low or optimal values are beneficial for the energy yield concerning different aspect.

| | Ground sky view factor | Unshaded ground fraction | Mutual shading | GNU |
|---|---|---|---|---|
| Distance | High | High | High | High |
| Height | Low | High | No influence | Optimal |

In summary, increasing the row-to-row distance of a bifacial PV farm is beneficial for the energy yield irrespective of the configuration whereas an optimal height value that maximizes the energy yield can be calculated depending on the location and the other design parameters. This is a combined result of the influence of $d$ and $h$ on individual aspects that affect the energy yield calculation, including sky view factor of the ground segments, unshaded ground fraction, mutual shading and non-uniformity of rear irradiance. Such relations are outlined in Table 1.

### 6.5. Economic potential of E/W vertical configuration

The profitability of E/W vertical with respect to N/S tilted configuration is studied in relation to six different variables:

(1) Max power fraction ($n_{max,power}$), which models a possible curtailment strategy and it is defined as the ratio between the maximum power allowed and the nominal power of the power plant.
(2) Ratio vertical/total modules ($n_{vert}$), which considers the possibility of "hybrid" PV farms where part of the modules are E/W vertical whereas the remaining are N/S tilted. It is expressed as the ratio between the number of vertical modules among the total.
(3) Row-to-row distance ($d$)
(4) Elevation of the modules ($h$)
(5) Minimum noon price ($p_{min}$)
(6) Price ratio ($p_{ratio}$)

The economic potential of vertical modules is quantified by the revenue gain ($R_{gain}$) while adopting the E/W vertical configuration instead of the N/S tilted counterpart, as shown in Eq. (19). Specifically,

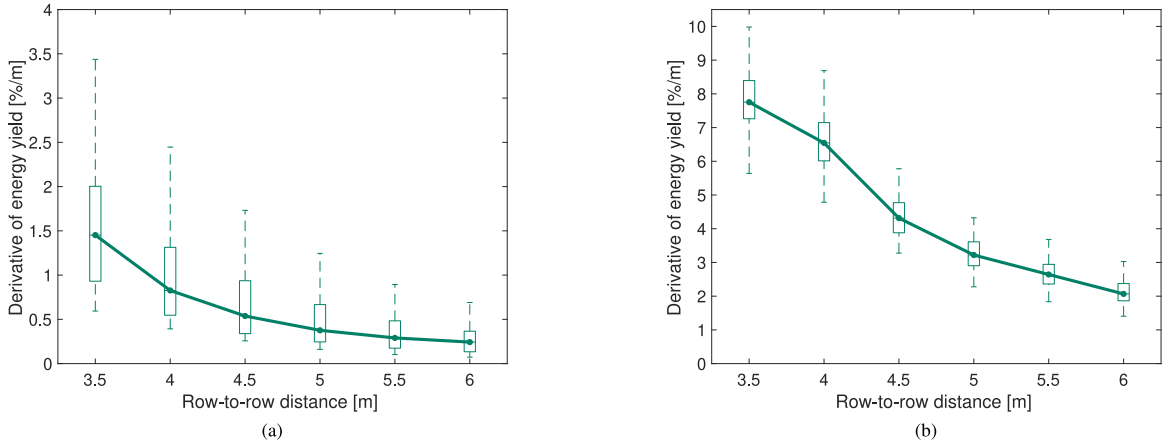


**Fig. 10.** Derivative of the energy yield with respect to the row-to-row distance ($\frac{\partial EY}{\partial d}$). The line represents the median values among the 102 different locations whereas maximum, minimum, 25th percentile and 75th percentile are represented through the boxplots. Both optimal tilt (a) and vertical (b) configurations are shown and a height of 1 m is considered.

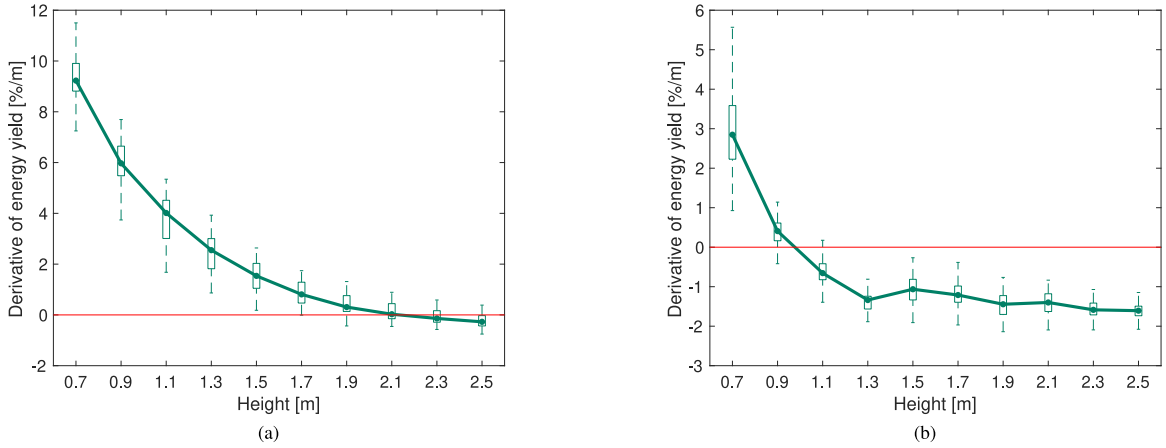


**Fig. 11.** Derivative of the energy yield with respect to the height ($\frac{\partial EY}{\partial h}$). The line represents the median values among the 102 different locations whereas maximum, minimum, 25th percentile and 75th percentile are represented through the boxplots. Both optimal tilt (a) and vertical (b) configurations are shown and a distance of 5 m is considered. The red line highlights the condition for the optimal height.

a positive $R_{gain}$ indicates that the E/W vertical is more profitable than the N/S tilted configuration under the specified conditions.

$$R_{gain} = \frac{R_{\text{new configuration}} - R_{\text{optimal tilt}}}{R_{\text{optimal tilt}}} \cdot 100\% \tag{19}$$

A preliminary assessment of the economic potential of the vertical configuration is performed by identifying the combination of $n_{max,power}$ and $n_{vert}$ that achieve a positive revenue gain ($R_{gain} > 0$). The results are visualized through contour plots, as illustrated in Fig. 12, which reports the examples of Utrecht and Madrid. The main focus of these graphs is to study the presence of "gain regions", i.e. areas in the graph where the condition $R_{gain} > 0$ is satisfied. Specifically, the enlargement of the gain regions when $d$ and $p_{ratio}$ are increased can be detected, proving the high sensitivity of E/W vertical modules profitability on these parameters. Overall, in the conditions shown in these examples vertical or hybrid PV farms appear to be favourable only in case a low $n_{max,power}$ is considered, which is not realistic due to the excessive energy curtailed.

To extend the analysis on a global perspective, the focus is shifted to the following question: *What is the minimum price ratio ($p_{ratio}$) required to achieve higher revenues using E/W vertical instead of N/S tilted PV modules ($R_{gain} > 0$)?* This $p_{ratio}$ value is studied for the different locations worldwide with respect to the following variables: $n_{max,power}$, $n_{vert}$, $d$, $h$ and $p_{min}$.

The curtailment strategy, expressed through $n_{max,power}$, has an influence on the minimum price ratio only for values $n_{max,power} < 0.7$, which entails significant power losses. Similarly, hybrid PV farms, described by $n_{vert}$ are found to be beneficial only in case of a heavy curtailment strategy ($n_{max,power} < 0.7$) is applied. Otherwise, either farms characterized by $n_{vert} = 0$ or $n_{vert=1}$ depending on market conditions and design parameters have to be preferred.

The same trend between the energy yield and the design parameters $d$ and $h$ is observed for the revenues, namely the highest revenues are obtained for larger $d$ and optimal $h$ values. Specifically, the influence of $p_{ratio}$ and $p_{min}$ is found to be minimal, i.e. less relevant than the interdependence of the design parameters. The sensitivity of the minimum $p_{ratio}$ to achieve the condition $R_{gain} > 0$ is depicted in Fig. 13 through global maps, where the green colour indicates the regions where the profitability of the vertical configuration is higher. It is observed that larger $d$ values increase the number of locations where E/W vertical modules are more profitable than N/S tilted configuration, proving the higher sensitivity on $d$ of vertical installations. On the other hand, small $h$ values seem to be beneficial for the profitability of the E/W vertical configuration, since lower $h_{opt}$ and minor impact of $h$ on the energy yield are observed for the vertical case. In general, the impact of $h$ is limited with respect to $d$ concerning the comparison between the two configurations. Even though the spatial diversification of the results highlighted in Fig. 13 suggests that the profitability of vertical modules is strictly dependent on the local climate, a slight trend can be recognized with the diffuse fraction. Specifically, a correlation analysis has highlighted that the locations characterized by a low diffuse fraction are favourable for E/W vertical configuration, resulting in higher values

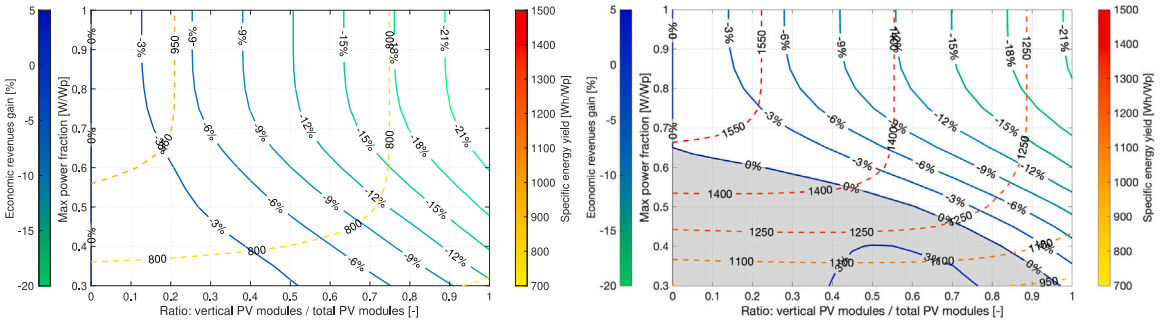


(a) Utrecht ($d = 3\,m$, $p_{ratio} = 2$) (b) Madrid ($d = 3\,m$, $p_{ratio} = 2$)

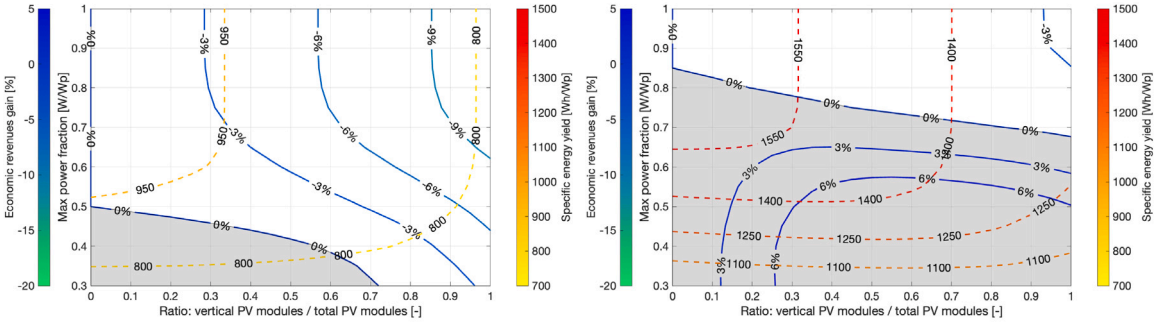


(c) Utrecht ($d = 4\,m$, $p_{ratio} = 5$) (d) Madrid ($d = 4\,m$, $p_{ratio} = 5$)

**Fig. 12.** Contour plots that show the energy yield and the revenue gain for different $n_{max,power}$ (y-axis) and $n_{vert}$ (x-axis) values, highlighted by the grey area ("gain region"). The examples of Utrecht and Madrid are presented. The other variables are set as follows: $h = 1$ m, $p_{min} = 200\,€/\text{MWh}$. These contour plots are generated by calculating the specific energy yield and the revenue gain for different conditions displayed in the axis or mentioned in the captions.

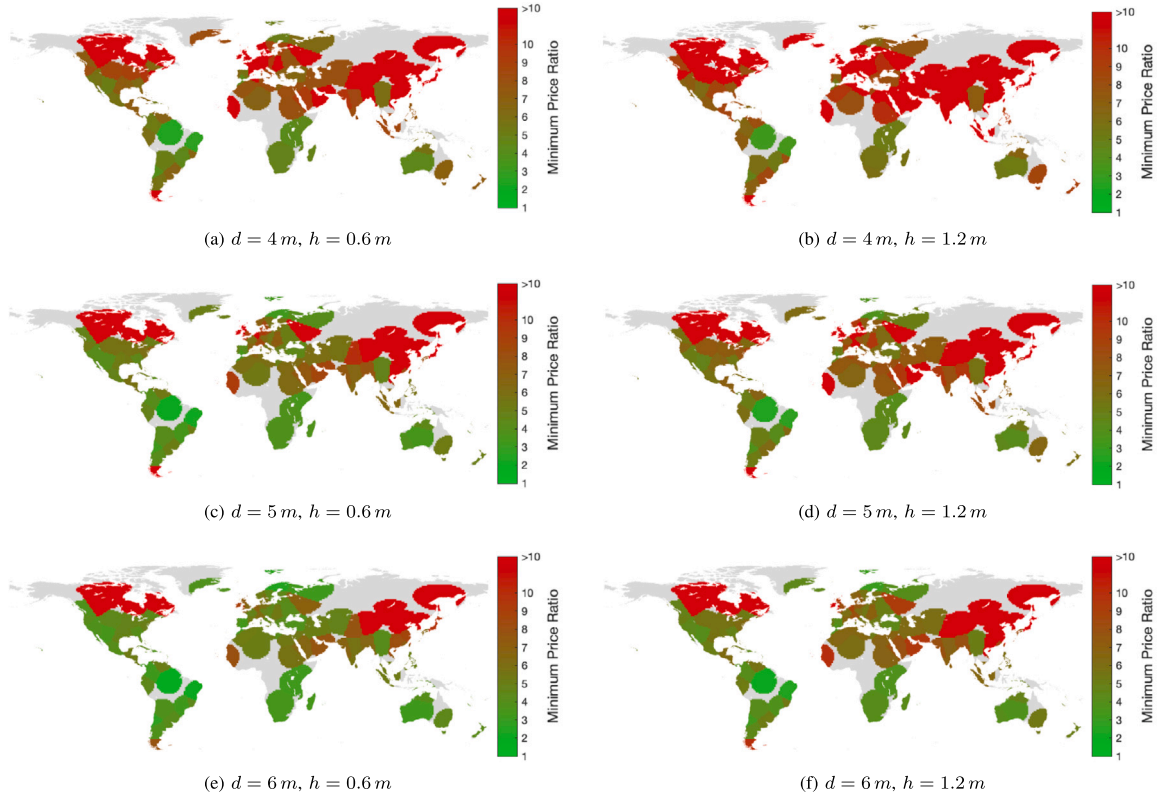


(a) $d = 4\,m$, $h = 0.6\,m$ (b) $d = 4\,m$, $h = 1.2\,m$

(c) $d = 5\,m$, $h = 0.6\,m$ (d) $d = 5\,m$, $h = 1.2\,m$

(e) $d = 6\,m$, $h = 0.6\,m$ (f) $d = 6\,m$, $h = 1.2\,m$

**Fig. 13.** Global maps of the minimum price ratio for which vertical modules are more profitable than tilted ones. The relevant variables are set as follows: $p_{min} = 100$ €/MWh, $n_{vert} = 1$, $n_{max,power} = 1$. (For interpretation of the references to colour in this figure legend, the reader is referred to the web version of this article.)

of $R_{gain}$. Such correlation increases (in absolute value) up to −0.7 when only morning/evening hours are considered.

With the exception of negative values, for which vertical configurations are always preferable, $p_{min}$ does not affect the values of $R_{gain}$.

**Table 2**
Influence of different variables on the minimum $p_{ratio}$ required to satisfy the condition $R_{gain} > 0$.

| Variable | Influence |
|---|---|
| $n_{max,power}$ | The influence is significant only in case of low $n_{max,power}$ values, which are not considered relevant for large-scale PV farms. |
| $n_{vert}$ | Hybrid PV farms are favourable only in case of low $n_{max,power}$, hence they are not relevant for this study. |
| $d$ | Large $d$ values increase the profitability of the vertical configuration over the tilted modules. |
| $h$ | $h$ values have a limited impact on the revenues, but lower values increase the profitability of vertical modules with respect to the tilted counterpart. |
| $p_{min}$ | Only the sign of the minimum price is relevant to decide the optimal configuration and vertical modules are always preferred in case of a negative $p_{min}$. |

This is caused by $R_{gain}$ definition since it is expressed in relative terms, as demonstrated in Appendix D. Lastly, Table 2 summarizes the results outlined in the previous paragraphs.

## 7. Conclusions and future work

The aim of this study was to investigate the potential of E/W vertical bifacial PV farms in terms of market revenues. Specifically, this configuration has been compared with the conventional N/S tilted counterpart and the analysis has been extended to a global scale. This has been achieved through the development of a bifacial PV farm model. This model has been validated using experimental data of the spatial irradiance incident on the rear side of the modules. MBD and RMSE between modelled and measured data amount to $-1.29$ W/m$^2$ ($-2.22\%$) and 12.65 W/m$^2$ (21.69%), respectively. Specifically, it has been observed that the design parameter that mostly affect the ability to predict the irradiance is the tilt and the error increases as the amount of unshaded ground seen by the specific cell increases, namely for high tilt values and at the edges of the modules. These results have confirmed the limitations of the view factor theory, which assumes all surfaces to be diffuse emitters.

Various market scenarios and installation conditions have been tested to determine their influence in the choice of the optimal configuration in terms of market revenues. The following conclusions have been drawn:

(1) The profitability of E/W vertical over the N/S tilted configuration is dependent on the design parameters, the curtailment strategy, the fraction of vertical modules in case of hybrid farms, the electricity market conditions and the specific location of the PV farm.
(2) The influence of the curtailment strategy is limited to the cases when the maximum power allowed is lower than 70% of the nominal power ($n_{max,power} < 0.7$).
(3) Hybrid PV farms which combine both configurations are beneficial only in case of heavy curtailment strategies, namely $n_{max,power} < 0.7$, otherwise either completely vertical or entirely tilted farms have to be preferred depending on the other parameters.
(4) Assuming an electricity price curve with a minimum around noon, the only market variable that affects the choice of the optimal configuration is the ratio between morning/evening and noon price. Therefore, the magnitude of the prices is not relevant in such decision whereas a minimum price ratio that guarantees higher profitability for vertical over tilted modules can be identified depending on the specific location and the other parameters.
(5) Larger row-to-row distance values increase the energy yield and the revenues of both vertical and tilted PV farms up to a saturation value. However, the impact of this parameter is higher for the former case hence an increase in the row-to-row distance fosters the profitability of E/W vertical over N/S tilted configurations.
(6) An optimal height that maximizes the energy yield for the vertical configuration depends on the specific location as well as the row-to-row distance. However, its impact on the decision of the optimal configuration is less relevant than the design parameters.
(7) There is a negative correlation between the revenue gain of vertical over tilted PV farms and the GHI-weighted average diffuse fraction of the locations. Therefore, vertical PV farms are favourable in locations characterized by a low diffuse fraction during morning and evening hours.

The exhaustiveness of this work is constrained by the computational resources and data available, preventing further investigation on the topic. The following guidelines aim to outline possible research pathways concerning this field.

(1) Time dependent albedo values could be adopted to further increase the reliability of the analysis, although the conclusions of the paper are not expected be impacted significantly.
(2) Even though the main limitations are intrinsic to the view factor concept, the use of corrective coefficients to include the effect of the mounting structure could be considered, in order to increase the accuracy of the rear irradiance estimation.
(3) To further improve the computational speed of the algorithm, the necessity of extending the dimensions of problem to consider effects like non-uniformity of the irradiance could be replaced by empirical coefficients. Their dependence on design and meteorological parameters could be investigated through machine learning techniques.
(4) Coupling with storage technologies should be considered to provide a wide overview of the profitability of E/W vertical configuration.

## Declaration of competing interest

The authors declare that they have no known competing financial interests or personal relationships that could have appeared to influence the work reported in this paper.

## Appendix A. Additional equations for bifacial PV farm model

### A.1. PV modules' shadows

Eqs. (20)–(22) are adopted to calculate the shadow of the modules on the ground, referring to Fig. 14.

$$y_1 = \frac{h - \frac{l}{2}\sin(\theta)}{\tan(\phi_s)} - \frac{l}{2}\cos(\theta) \tag{20}$$

$$y_2 = \frac{h + \frac{l}{2}\sin(\theta)}{\tan(\phi_s)} + \frac{l}{2}\cos(\theta) \tag{21}$$

$$\phi_s = \max\left[0, \arctan\left(\frac{\tan(a_s)}{\cos(A_m - A_s)}\right)\right] \tag{22}$$

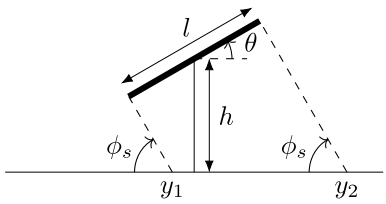


**Fig. 14.** Extremes of the shadow on the ground.

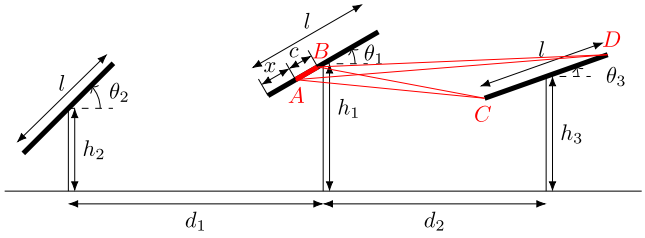


**Fig. 15.** View factor between a cell and the neighbouring module.

### A.2. View factor between PV cell and ground segment

The expression (23)–(26) are used to calculate the length of the segments included in Eq. (9), referring to Fig. 3(b).

$$AC = \sqrt{(h + (x - \frac{l}{2})\sin\theta)^2 + (y_1 - (x - \frac{l}{2})\cos\theta)^2} \tag{23}$$

$$AD = \sqrt{(h + (x - \frac{l}{2})\sin\theta)^2 + (y_2 - (x - \frac{l}{2})\cos\theta)^2} \tag{24}$$

$$BC = \sqrt{(h + (x - \frac{l}{2} + c)\sin\theta)^2 + (y_1 - (x - \frac{l}{2} + c)\cos\theta)^2} \tag{25}$$

$$BD = \sqrt{(h + (x - \frac{l}{2} + c)\sin\theta)^2 + (y_2 - (x - \frac{l}{2} + c)\cos\theta)^2} \tag{26}$$

### A.3. View factor between PV cells and neighbouring modules

The view factor between PV cells and neighbouring modules ($VF_{c\to m}$) are calculated according to the expression (27), where the segments are obtained from the coordinates included in the Eqs. (28)–(31), as illustrated in Fig. 15. Taking into account the possibility of unconventional configurations adds complexity to these equations. Specifically, symbols $\xi_1$ and $\xi_2$ indicate the angles between the lines that connect the extremes of the cell and the neighbouring modules and the vertical direction.

$$VF_{c\to m} = \frac{BC + AD - AC - BC}{2 \cdot c} \tag{27}$$

$$\begin{cases} x_a = (x - \frac{l}{2}) \cdot \cos(\theta_1) \\ y_a = h_1 + (x - \frac{l}{2}) \cdot \sin(\theta_1); \end{cases} \tag{28}$$

$$\begin{cases} x_b = (x - \frac{l}{2} + c) \cdot \cos(\theta_1) \\ y_b = h_1 + (x - \frac{l}{2} + c) \cdot \sin(\theta_1); \end{cases} \tag{29}$$

$$\begin{cases} x_c = \frac{-\tan(\xi_1 - \frac{\pi}{2}) \cdot x_a + y_a + \tan(\theta_2) \cdot d_2 - h_3}{\tan(\theta_2) - \tan(\xi_1 - \frac{\pi}{2})} \\ y_c = \tan(\theta_3) \cdot (x_c - d_2) + h_3 \end{cases} \tag{30}$$

$$\begin{cases} x_d = \frac{-\tan(\xi_2 - \frac{\pi}{2}) \cdot x_b + y_b + \tan(\theta_3) \cdot d_2 - h_3}{\tan(\theta_3) - \tan(\xi_2 - \frac{\pi}{2})} \\ y_d = \tan(\theta_3) \cdot (x_d - d_2) + h_3 \end{cases} \tag{31}$$

**Table 3**
Design parameters used for the validation.

| Design parameter | Value |
|---|---|
| Length | 2.14 m |
| Orientation | 187 °N |
| Height (from the bottom extreme) | 0.5 m |
| Row-to-row distance | 4.3 m – 4.8 m – 5 m |

**Table 4**
Time periods selected for the model's validation and the correspondent installation conditions.

| Time period | Weather | Ground type | Albedo | Tilt |
|---|---|---|---|---|
| 28-7-2020 15.30–18.15 | Cloudy | White fleece | 0.53 | 30° |
| 29-7-2020 10.00–18.00 | Cloudy | White fleece | 0.53 | 30° |
| 30-7-2020 11.00–18.00 | Sunny | White fleece | 0.53 | 30° |
| 31-7-2020 11.30–15.30 | Sunny | Artificial grass | 0.13 | 30° |
| 1-8-2020 10.00–18.00 | Cloudy | Stones | 0.19 | 30° |
| 2-8-2020 10.00–18.00 | Sunny | Stones | 0.19 | 30° |
| 3-8-2020 10.00–18.00 | Rainy | Stones | 0.15 | 30° |
| 4-8-2020 10.00–18.00 | Sunny | Stones | 0.19 | 45° |
| 1-9-2020 14.00–18.00 | Cloudy | White fleece (wet) | 0.50 | 52° |
| 6-9-2020 9.00–19.00 | N.A. | White fleece (wet) | 0.45 | 52° |
| 7-9-2020 12.30–19.00 | Cloudy | White fleece (wet) | 0.50 | 52° |
| 13-9-2020 9.00–19.00 | Sunny | Stones | 0.18 | 52° |

### A.4. Temperature of PV cells: INOCT model

Eqs. (32)–(36) [51,56] are used to estimate the cells temperature using INOCT model, where rack mounting installations are considered.

$$T_{INOCT} = T_{NOCT} - 3 \tag{32}$$

$$T_{cell} = T_{amb} + \frac{G_{tot}}{G_{NOCT}} \cdot \left(T_{INOCT} - 20\ °\mathrm{C}\right) \tag{33}$$

$$G_{front} = \int_{\lambda_1}^{\lambda_2} [I_{front,sky}(\lambda) + I_{front,ground}(\lambda) + I_{front,mod}(\lambda)]\, d\lambda \tag{34}$$

$$G_{rear} = \int_{\lambda_1}^{\lambda_2} [I_{rear,sky}(\lambda) + I_{rear,ground}(\lambda) + I_{rear,mod}(\lambda)]\, d\lambda \tag{35}$$

$$G_{tot} = G_{front} + G_{rear} \tag{36}$$

## Appendix B. Experimental validation: additional data

Tables 3, 4, 5 include the installation conditions and the detailed results of the validation process. Table 6 contains the information concerning the sensors adopted during the experimental validation.

## Appendix C. Specification of the modules

Table 7 summarizes the specifications of the modules adopted for the simulations.

## Appendix D. Influence of $p_{min}$ on the profitability of e/w vertical over n/s tilted configuration

The minimum price influences the revenues gain in absolute terms but has no impact when relative metrics are adopted, as explained through an example. Let us consider two different electricity price curves $e_1(t)$ and $e_2(t)$ modelled as described in Section 4. Suppose that are characterized by the same price ratio ($p_{ratio,1} = p_{ratio,2}$) but two

**Table 5**
Validation results: RMSE and MBD between modelled and measured data for the selected days.

| Day | Unit | Sensor 1 (bottom) | | Sensor 2 | | Sensor 3 | | Sensor 4 | | Sensor 5 | | Sensor 6 (top) | |
|---|---|---|---|---|---|---|---|---|---|---|---|---|---|
| | | RMSE | MBD | RMSE | MBD | RMSE | MBD | RMSE | MBD | RMSE | MBD | RMSE | MBD |
| 28-7-2020 | [W/m$^2$] | 5.99 | −5.43 | 8.93 | −8.17 | 9.13 | −8.24 | 6.51 | −4.98 | 4.53 | −1.78 | 4.28 | 1.14 |
| | [%] | 9.07 | −8.21 | 14.76 | −13.51 | 15.04 | −13.56 | 10.31 | −7.90 | 6.89 | −2.70 | 6.19 | 1.64 |
| 29-7-2020 | [W/m$^2$] | 12.04 | −4.15 | 17.22 | −13.43 | 18.02 | −15.12 | 16.29 | −12.60 | 13.94 | −9.04 | 13.44 | −6.02 |
| | [%] | 11.28 | −3.89 | 18.60 | −14.51 | 20.10 | −16.87 | 17.42 | −13.47 | 13.96 | −9.06 | 12.39 | −5.55 |
| 30-7-2020 | [W/m$^2$] | 11.99 | −7.68 | 25.28 | −23.89 | 26.56 | −25.64 | 25.77 | −24.77 | 22.44 | −21.38 | 21.84 | −20.48 |
| | [%] | 7.60 | −4.87 | 20.69 | −19.54 | 24.83 | −23.97 | 23.93 | −23.00 | 19.24 | −18.33 | 16.41 | −15.39 |
| 31-7-2020 | [W/m$^2$] | 8.62 | 8.47 | 0.94 | 0.44 | 4.85 | −4.83 | 6.39 | −6.37 | 6.30 | −6.29 | 5.56 | −5.54 |
| | [%] | 22.83 | 22.42 | 3.07 | 1.43 | 15.74 | −15.66 | 19.15 | −19.11 | 16.73 | −16.69 | 12.87 | −12.83 |
| 1-8-2020 | [W/m$^2$] | 4.61 | −1.98 | 4.35 | −2.21 | 4.46 | −2.86 | 4.63 | −2.25 | 4.41 | −1.21 | 4.99 | 0.78 |
| | [%] | 12.78 | −5.48 | 14.82 | −7.54 | 15.51 | −9.95 | 15.11 | −7.34 | 13.29 | −3.65 | 14.04 | 2.20 |
| 2-8-2020 | [W/m$^2$] | 6.96 | −1.71 | 5.76 | −2.28 | 5.70 | −3.02 | 6.04 | −2.22 | 5.91 | −1.02 | 6.71 | 0.97 |
| | [%] | 13.79 | −3.39 | 14.56 | −5.78 | 15.14 | −8.03 | 15.20 | −5.59 | 13.57 | −2.34 | 14.02 | 2.02 |
| 3-8-2020 | [W/m$^2$] | 2.02 | 0.42 | 1.78 | −0.08 | 2.17 | −0.65 | 2.71 | −0.01 | 3.25 | 0.81 | 4.44 | 2.44 |
| | [%] | 16.36 | 3.37 | 15.42 | −0.74 | 17.55 | −5.30 | 20.52 | −0.09 | 23.32 | 5.80 | 31.59 | 17.36 |
| 4-8-2020 | [W/m$^2$] | 5.08 | −3.80 | 4.61 | −3.50 | 5.98 | −4.81 | 5.53 | −3.90 | 4.99 | −2.26 | 5.45 | 2.87 |
| | [%] | 8.06 | −6.04 | 9.00 | −6.83 | 11.88 | −9.56 | 10.37 | −7.30 | 8.69 | −3.94 | 9.32 | 4.92 |
| 1-9-2020 | [W/m$^2$] | 11.13 | −10.77 | 9.31 | −8.86 | 8.90 | −8.43 | 6.57 | −5.91 | 3.91 | −2.34 | 5.93 | 4.38 |
| | [%] | 25.98 | −25.13 | 22.22 | −21.16 | 20.74 | −19.65 | 15.44 | −13.88 | 9.64 | −5.78 | 16.75 | 12.37 |
| 6-9-2020 | [W/m$^2$] | 21.03 | −1.38 | 16.65 | 0.70 | 14.81 | 3.52 | 16.52 | 8.29 | 20.21 | 14.35 | 28.32 | 23.93 |
| | [%] | 24.47 | −1.60 | 23.26 | 0.97 | 23.19 | 5.51 | 27.27 | 13.69 | 34.98 | 24.83 | 54.27 | 45.87 |
| 7-9-2020 | [W/m$^2$] | 9.61 | −6.09 | 8.23 | −3.22 | 7.97 | 0.45 | 10.34 | 5.88 | 16.36 | 13.91 | 27.02 | 24.90 |
| | [%] | 7.87 | −4.98 | 8.25 | −3.22 | 9.16 | 0.51 | 12.71 | 7.23 | 21.40 | 18.19 | 38.68 | 35.66 |
| 13-9-2020 | [W/m$^2$] | 5.22 | 4.07 | 6.67 | 5.86 | 6.24 | 5.39 | 7.67 | 6.85 | 9.88 | 9.11 | 17.96 | 16.85 |
| | [%] | 11.75 | 9.16 | 17.52 | 15.37 | 16.75 | 14.47 | 20.23 | 18.08 | 25.65 | 23.64 | 52.24 | 49.01 |

**Table 6**
Sensors adopted for the measurements.

| Kipp&Zonen sensor | Variable measured | Classification ISO 9060:2018 |
|---|---|---|
| SP Lite2 | Rear irradiance at different positions | Class C |
| RaZON+ | $DNI$, $DHI$, $GHI$ | Class C |

**Table 7**
PV module specifications adopted in this study, based on the product LG400N2T-A5.

| Parameter | Value |
|---|---|
| Dimensions of the module ($w \cdot l$) | 2.064 × 1.024 m |
| Cells configuration | 6 × 12 |
| Bypass diodes | 3 |
| Cell's length ($c$) | 0.1707 m |
| Rated power ($P_{rated}$) | 440 Wp |
| Short-circuit current ($I_{sc,STC}$) | 11.24 A |
| Open-circuit voltage $V_{oc,STC}$ | 49.7 V |
| Series-connected cells ($N_s$) | 72 |
| Parallel-connected cells ($N_p$) | 1 |
| NOCT Temperature ($T_{NOCT}$) | 45 °C |
| Temperature coefficient for $I_{sc}$ ($k_{I_{sc}}$) | 0.03%/C |
| Temperature coefficient for $V_{oc}$ ($k_{V_{oc}}$) | −0.27%/C |
| Ideality factor ($n$) | 2 |
| Reflectivity ($r$) | 10% |

different (positive) minimum noon prices ($p_{min,1} \neq p_{min,2}$). According to their definition, the relation between $e_1(t)$ and $e_2(t)$ expressed in Eq. (37) is valid.

$$e_1(t) = \frac{p_{min,1}}{p_{min,2}} \cdot e_2(t) \tag{37}$$

The revenues of the vertical and the tilted configuration obtained for the market conditions described by $e_1(t)$ are indicated with $R_{v,1}$ and $R_{t,1}$. Similarly, $R_{v,2}$ and $R_{t,2}$ refer to $e_2(t)$ electricity price curve. The revenue gain can be obtained as shown in Eqs. (38) and (39), where $P_v(t)$ and $P_t(t)$ are the power curves of the vertical and tilted farm during the time period $[t_1, t_2]$.

$$R_{gain,1} = \frac{R_{v,1} - R_{t,1}}{R_{t,1}} = \frac{R_{v,1}}{R_{t,1}} - 1 = \frac{\int_{t_1}^{t_2} e_1(t) P_v(t) dt}{\int_{t_1}^{t_2} e_1(t) P_t(t) dt} - 1 \tag{38}$$

$$R_{gain,2} = \frac{R_{v,2} - R_{t,2}}{R_{t,2}} = \frac{R_{v,2}}{R_{t,2}} - 1 = \frac{\int_{t_1}^{t_2} e_2(t) P_v(t) dt}{\int_{t_1}^{t_2} e_2(t) P_t(t) dt} - 1 \tag{39}$$

Therefore, combining the relations (37)–(39), the condition illustrated in Eq. (40) is derived, proving the validity of the statement concerning the impact of $p_{min}$ on the results.

$$\begin{aligned} R_{gain,1} &= \frac{\int_{t_1}^{t_2} e_1(t) P_v(t) dt}{\int_{t_1}^{t_2} e_1(t) P_t(t) dt} - 1 \\ &= \frac{\int_{t_1}^{t_2} \left[\frac{p_{min,1}}{p_{min,2}} \cdot e_2(t)\right] P_v(t) dt}{\int_{t_1}^{t_2} \left[\frac{p_{min,1}}{p_{min,2}} \cdot e_2(t)\right] P_t(t) dt} - 1 \\ &= \frac{\cancel{\frac{p_{min,1}}{p_{min,2}}} \cdot \int_{t_1}^{t_2} e_2(t) P_v(t) dt}{\cancel{\frac{p_{min,1}}{p_{min,2}}} \cdot \int_{t_1}^{t_2} e_2(t) P_t(t) dt} - 1 \\ &= \frac{\int_{t_1}^{t_2} e_2(t) P_v(t) dt}{\int_{t_1}^{t_2} e_2(t) P_t(t) dt} - 1 = R_{gain,2} \end{aligned} \tag{40}$$

## References


[1] IRENA, World Energy Transitions Outlook 2023: 1.5° C Pathway, Tech. Rep., International Renewable Energy Agency, Abu Dhabi, 2023.

[2] M. Fischer, M. Woodhouse, P. Baliozian, J. Trube, International Technology Roadmap for Photovoltaics (ITRPV) 14th Edition: 2022 Results, Tech. Rep., 2023, [Online]. Available: https://www.vdma.org/.

[3] R. Kopecek, J. Libal, Towards large-scale deployment of bifacial photovoltaics, Nat. Energy 3 (2018) 443–446, [Online]. Available: https://doi.org/10.1038/s41560-018-0178-0.

[4] J. Manuel Longares, A. García-Jiménez, N. García-Polanco, Multiphysics simulation of bifacial photovoltaic modules and software comparison, Sol. Energy 257 (2023) 155–163, [Online]. Available: https://www.sciencedirect.com/science/article/pii/S0038092X23002244.

[5] C.D. Rodríguez-Gallegos, H. Liu, O. Gandhi, J.P. Singh, V. Krishnamurthy, A. Kumar, J.S. Stein, S. Wang, L. Li, T. Reindl, I.M. Peters, Global techno-economic performance of bifacial and tracking photovoltaic systems, Joule 4 (7) (2020) 1514–1541, [Online]. Available: https://www.sciencedirect.com/science/article/pii/S2542435120301884.

[6] E. Mouhib, L. Micheli, F.M. Almonacid, E.F. Fernández, Overview of the fundamentals and applications of bifacial photovoltaic technology: Agrivoltaics and aquavoltaics, Energies 15 (23) (2022) [Online]. Available: https://www.scopus.com/inward/record.uri?eid=2-s2.0-85143786369&doi=10.3390%2fen15238777&partnerID=40&md5=f096e76762a191431bbb8ed68c5d038f.

[7] B. Marion, S. MacAlpine, C. Deline, A. Asgharzadeh, F. Toor, D. Riley, J. Stein, C. Hansen, A practical irradiance model for bifacial PV modules, in: 2017 IEEE 44th Photovoltaic Specialist Conference, PVSC, Washington, DC, USA, 2017, pp. 1537–1542.

[8] S.A. Pelaez, C. Deline, S.M. MacAlpine, B. Marion, J.S. Stein, R.K. Kostuk, Comparison of bifacial solar irradiance model predictions with field validation, IEEE J. Photovolt. 9 (1) (2019) 82–88.

[9] G.J. Ward, The Radiance Lighting Simulation and Rendering System, Association for Computing Machinery, New York, NY, USA, 1994, pp. 459–472, [Online]. Available: https://doi.org/10.1145/192161.192286.

[10] G. Raina, S. Sinha, A comprehensive assessment of electrical performance and mismatch losses in bifacial PV module under different front and rear side shading scenarios, Energy Convers. Manage. 261 (2022) 115668, [Online]. Available: https://www.sciencedirect.com/science/article/pii/S0196890422004642.

[11] E. Mouhib, P.M. Rodrigo, L. Micheli, E.F. Fernández, F. Almonacid, Quantifying the rear and front long-term spectral impact on bifacial photovoltaic modules, Sol. Energy 247 (2022) 202–213, [Online]. Available: https://www.sciencedirect.com/science/article/pii/S0038092X2200768X.

[12] S. Ayala Pelaez, C. Deline, J.S. Stein, B. Marion, K. Anderson, M. Muller, Effect of torque-tube parameters on rear-irradiance and rear-shading loss for bifacial PV performance on single-axis tracking systems, in: 2020 IEEE 46th Photovoltaic Specialists Conference, PVSC, 2020, [Online]. Available: https://www.osti.gov/biblio/1726058.

[13] C.D. Rodríguez-Gallegos, M. Bieri, O. Gandhi, J.P. Singh, T. Reindl, S. Panda, Monofacial vs bifacial si-based PV modules: Which one is more cost-effective? Sol. Energy 176 (2018) 412–438, [Online]. Available: https://www.sciencedirect.com/science/article/pii/S0038092X18309915.

[14] E.M. Tonita, A.C. Russell, C.E. Valdivia, K. Hinzer, Optimal ground coverage ratios for tracked, fixed-tilt, and vertical photovoltaic systems for latitudes up to 75°N, Sol. Energy 258 (2023) 8–15, [Online]. Available: https://www.scopus.com/inward/record.uri?eid=2-s2.0-85154539477&doi=10.1016%2fj.solener.2023.04.038&partnerID=40&md5=09d69f53fd0d7ac400596d348d6bbd4a.

[15] O.A. Katsikogiannis, H. Ziar, O. Isabella, Integration of bifacial photovoltaics in agrivoltaic systems: A synergistic design approach, Appl. Energy 309 (2022) 118475, [Online]. Available: https://www.sciencedirect.com/science/article/pii/S0306261921016986.

[16] H. Alam, M.A. Alam, N.Z. Butt, Techno economic modeling for agrivoltaics: Can agrivoltaics be more profitable than ground mounted pv? IEEE J. Photovolt. 13 (1) (2023) 174–186.

[17] R. Arena, S. Aneli, A. Gagliano, G.M. Tina, Optimal photovoltaic array layout of agrivoltaic systems based on vertical bifacial photovoltaic modules, Solar RRL 8 (1) (2024) [Online]. Available: https://www.scopus.com/inward/record.uri?eid=2-s2.0-85178111452&doi=10.1002%2fsolr.202300505&partnerID=40&md5=0987115367cfa3db5df490c8ee1a3efa.

[18] R. Bruhwyler, H. Sánchez, C. Meza, F. Lebeau, P. Brunet, G. Dabadie, S. Dittmann, R. Gottschalg, J.J. Negroni, Vertical agrivoltaics and its potential for electricity production and agricultural water demand: A case study in the area of Chanco, Chile, Sustain. Energy Technol. Assess. 60 (2023) [Online]. Available: https://www.scopus.com/inward/record.uri?eid=2-s2.0-85171330054&doi=10.1016%2fj.seta.2023.103425&partnerID=40&md5=ee51e77ea250dc52e2188fe86af5217b.

[19] K. Ali Khan Niazi, M. Victoria, Comparative analysis of photovoltaic configurations for agrivoltaic systems in Europe, Prog. Photovolt., Res. Appl. 31 (11) (2023) 1101–1113, [Online]. Available: https://www.scopus.com/inward/record.uri?eid=2-s2.0-85165284216&doi=10.1002%2fpip.3727&partnerID=40&md5=38b1c6c1b32e491277275d0178d32154.

[20] U. Jamil, A. Bonnington, J.M. Pearce, The agrivoltaic potential of Canada, Sustainability (Switzerland) 15 (4) (2023) [Online]. Available: https://www.scopus.com/inward/record.uri?eid=2-s2.0-85149240130&doi=10.3390%2fsu15043228&partnerID=40&md5=ee4b1c3d74414735f23e8a34a02c36da.

[21] A. Singhal, G. Raina, D.K. Meena, S. Sinha, Technical feasibility of agro-photovoltaic system in composite climate of India for future sustainability, in: 2023 IEEE 3rd International Conference on Sustainable Energy and Future Electric Transportation, SeFet 2023, 2023, [Online]. Available: https://www.scopus.com/inward/record.uri?eid=2-s2.0-85173604284&doi=10.1109%2fSeFeT57834.2023.10244926&partnerID=40&md5=f6a48de325afaf13473dc650bf35fa66.

[22] S.G. Gulhane, A. Phadke, Design of agro-photovoltaic system for optimized energy generation and crop yield using fuzzy framework, in: 2023 2nd International Conference for Innovation in Technology, INOCON 2023, 2023, [Online]. Available: https://www.scopus.com/inward/record.uri?eid=2-s2.0-85158068075&doi=10.1109%2fINOCON57975.2023.10101340&partnerID=40&md5=f336f03436da77fe918960ce49b737d1.

[23] U.B. Qasim, M.H. Riaz, H. Imran, Investigation of soiling effects for east/west vertical bifacial and north/south tilted monofacial photovoltaic farms, Energy Environ. (2023) [Online]. Available: https://www.scopus.com/inward/record.uri?eid=2-s2.0-85147446911&doi=10.1177%2f0958305X221143410&partnerID=40&md5=b5fff9ab4eb4ead09a8073a34694e0d8.

[24] M.H. Riaz, H. Imran, H. Alam, M.A. Alam, N.Z. Butt, Crop-specific optimization of bifacial PV arrays for agrivoltaic food-energy production: The light-productivity-factor approach, IEEE J. Photovolt. 12 (2) (2022) 572–580, [Online]. Available: https://www.scopus.com/inward/record.uri?eid=2-s2.0-85122869383&doi=10.1109%2fJPHOTOV.2021.3136158&partnerID=40&md5=be79e789c739d1b9c6c721d658d78836.

[25] H. Imran, M.H. Riaz, Investigating the potential of east/west vertical bifacial photovoltaic farm for agrivoltaic systems, J. Renew. Sustain. Energy 13 (3) (2021) [Online]. Available: https://www.scopus.com/inward/record.uri?eid=2-s2.0-85108712348&doi=10.1063%2f5.0054085&partnerID=40&md5=1ec345dfb170ea5341907d8aab853425.

[26] G. Faturrochman, M. de Jong, R. Santbergen, W. Folkerts, M. Zeman, A. Smets, Maximizing annual yield of bifacial photovoltaic noise barriers, Sol. Energy 162 (2018) 300–305, [Online]. Available: https://www.sciencedirect.com/science/article/pii/S0038092X1830001X.

[27] L. Soares, H. Wang, Sustainability impact of photovoltaic noise barriers with different design configurations, Transp. Res. D 116 (2023) [Online]. Available: https://www.scopus.com/inward/record.uri?eid=2-s2.0-85147195257&doi=10.1016%2fj.trd.2023.103624&partnerID=40&md5=6188c87b2d3362f5aa81f4705bc46acb.

[28] J. Peerlings, A. Reinders, C. Catita, M.C. Brito, The photovoltaic potential for electric vehicle charging along highways: A dutch case study, Prog. Photovolt., Res. Appl. (2023) [Online]. Available: https://www.scopus.com/inward/record.uri?eid=2-s2.0-85178463804&doi=10.1002%2fpip.3759&partnerID=40&md5=523acaa285b1a51b09b373100d2fdb50.

[29] G. Raina, S. Sinha, Experimental investigations of front and rear side soiling on bifacial PV module under different installations and environmental conditions, Energy Sustain. Dev. 72 (2023) 301–313, [Online]. Available: https://www.scopus.com/inward/record.uri?eid=2-s2.0-85146433828&doi=10.1016%2fj.esd.2023.01.001&partnerID=40&md5=02d022124f91b9b50716dfb875ffff7e.

[30] S. Jouttijärvi, J. Thorning, M. Manni, H. Huerta, S. Ranta, M. Di Sabatino, G. Lobaccaro, K. Miettunen, A comprehensive methodological workflow to maximize solar energy in low-voltage grids: A case study of vertical bifacial panels in nordic conditions, Sol. Energy 262 (2023) [Online]. Available: https://www.scopus.com/inward/record.uri?eid=2-s2.0-85163872353&doi=10.1016%2fj.solener.2023.111819&partnerID=40&md5=d6dcbcc868d90588676c055a29b6c601.

[31] S. Jouttijärvi, G. Lobaccaro, A. Kamppinen, K. Miettunen, Benefits of bifacial solar cells combined with low voltage power grids at high latitudes, Renew. Sustain. Energy Rev. 161 (2022) [Online]. Available: https://www.scopus.com/inward/record.uri?eid=2-s2.0-85126924001&doi=10.1016%2fj.rser.2022.112354&partnerID=40&md5=cf8673d5572ee8b4699be6d695702843.

[32] S. Obara, D. Konno, Y. Utsugi, J. Morel, Analysis of output power and capacity reduction in electrical storage facilities by peak shift control of PV system with bifacial modules, Appl. Energy 128 (2014) 35–48, [Online]. Available: https://www.sciencedirect.com/science/article/pii/S0306261914004061.

[33] S.-M. Lee, E.-C. Lee, J.-H. Lee, S.-H. Yu, J.-S. Heo, W.-Y. Lee, B.-S. Kim, Analysis of the output characteristics of a vertical photovoltaic system based on operational data: A case study in Republic of Korea, Energies 16 (19) (2023) [Online]. Available: https://www.scopus.com/inward/record.uri?eid=2-s2.0-85173829473&doi=10.3390%2fen16196971&partnerID=40&md5=4250b81825f08fb4630525cace3adefb.

[34] R. Shigenobu, M. Ito, H. Taoka, Optimal design of bifacial PV system to mitigate duck-curve problem of power system with the UC problem, Energy Rep. 7 (2021) 7004–7014, [Online]. Available: https://www.sciencedirect.com/science/article/pii/S2352484721010775.

[35] ENTSO-E transparency platform, 2023, https://transparency.entsoe.eu/. Accessed on May 15, 2023.

[36] G. Raina, S. Sinha, A holistic review approach of design considerations, modelling, challenges and future applications for bifacial photovoltaics, Energy Convers. Manage. 271 (2022) 116290, [Online]. Available: https://www.sciencedirect.com/science/article/pii/S0196890422010676.

[37] D. Chudinzow, S. Nagel, J. Güsewell, L. Eltrop, Vertical bifacial photovoltaics – A complementary technology for the European electricity supply? Appl. Energy 264 (2020) 114782, [Online]. Available: https://www.sciencedirect.com/science/article/pii/S0306261920302944.

[38] T. Bergman, Fundamentals of Heat and Mass Transfer, Wiley, 2011, [Online]. Available: https://books.google.nl/books?id=vvyIoXEywMoC.

[39] W. Nusselt, Graphische Bestimmung der Winkelverhaltwisses Beider Warmestrahlang, Vol. 72, 1928, p. 673.

[40] M. Mirhosseini, A. Saboonchi, View factor calculation using the Monte Carlo method for a 3D strip element to circular cylinder, Int. Commun. Heat Mass Transfer 38 (6) (2011) 821–826, [Online]. Available: https://www.sciencedirect.com/science/article/pii/S0735193311000674.

[41] H.C. Hottel, A.F. Sarofin, Radiative Transfer, McGraw Hill, New York, 1967, pp. 31–39.

[42] F.F. Sönmez, H. Ziar, O. Isabella, M. Zeman, Fast and accurate ray-casting-based view factor estimation method for complex geometries, Sol. Energy Mater. Sol. Cells 200 (2019) 109934, [Online]. Available: https://www.sciencedirect.com/science/article/pii/S0927024819302557.

[43] C. Deline, S. MacAlpine, B. Marion, F. Toor, A. Asgharzadeh, J.S. Stein, Assessment of bifacial photovoltaic module power rating methodologies—Inside and out, IEEE J. Photovolt. 7 (2) (2017) 575–580.

[44] S.A. Pelaez, C. Deline, Bifacial_radiance: a python package for modeling bifacial solar photovoltaic systems, J. Open Source Softw. 5 (50) (2020) 1865, [Online]. Available: https://doi.org/10.21105/joss.01865.

[45] A. Asgharzadeh, M.A. Anoma, A. Hoffman, C. Chaudhari, S. Bapat, R. Perkins, D. Cohen, G.M. Kimball, D. Riley, F. Toor, B. Bourne, A benchmark and validation of bifacial PV irradiance models, in: 2019 IEEE 46th Photovoltaic Specialists Conference, PVSC, 2019, pp. 3281–3287.

[46] C. Deline, S. Ayala Pelaez, S. MacAlpine, C. Olalla, Estimating and parameterizing mismatch power loss in bifacial photovoltaic systems, Prog. Photovolt., Res. Appl. 28 (7) (2020) 691–703, [Online]. Available: https://onlinelibrary.wiley.com/doi/abs/10.1002/pip.3259.

[47] J. Ledesma, R. Almeida, F. Martinez-Moreno, C. Rossa, J. Martín-Rueda, L. Narvarte, E. Lorenzo, A simulation model of the irradiation and energy yield of large bifacial photovoltaic plants, Sol. Energy 206 (2020) 522–538, [Online]. Available: https://www.sciencedirect.com/science/article/pii/S0038092X20306071.

[48] N. Riedel-Lyngskær, M. Ribaconka, M. Pó, S. Thorsteinsson, A. Thorseth, C. Dam-Hansen, M.L. Jakobsen, Spectral albedo in bifacial photovoltaic modeling: What can be learned from onsite measurements? in: 2021 IEEE 48th Photovoltaic Specialists Conference, PVSC, 2021, pp. 0942–0949.

[49] N. Riedel-Lyngskær, M. Ribaconka, M. Pó, A. Thorseth, S. Thorsteinsson, C. Dam-Hansen, M.L. Jakobsen, The effect of spectral albedo in bifacial photovoltaic performance, Sol. Energy 231 (2022) 921–935, [Online]. Available: https://www.sciencedirect.com/science/article/pii/S0038092X21010720.

[50] M.R. Vogt, T. Gewohn, K. Bothe, C. Schinke, R. Brendel, Impact of using spectrally resolved ground albedo data for performance simulations of bifacial modules, in: Proc. 35th Eur. Photovolt. Sol. Energy Conf., 2018, pp. 1011–1016.

[51] M.K. Fuentes, A simplified thermal model for flat-plate photovoltaic arrays, 1987, [Online]. Available: https://www.osti.gov/biblio/6802914.

[52] J.A. Kratochvil, W.E. Boyson, D.L. King, Photovoltaic Array Performance Model, Tech. Rep., Sandia National Laboratories, New Mexico, 2004, [Online]. Available: http://dx.doi.org/10.2172/919131.

[53] D. Faiman, Assessing the outdoor operating temperature of photovoltaic modules, Prog. Photovolt., Res. Appl. 16 (4) (2008) 307–315, [Online]. Available: https://onlinelibrary.wiley.com/doi/abs/10.1002/pip.813.

[54] G.J. Janssen, B.B. Van Aken, A.J. Carr, A.A. Mewe, Outdoor performance of bifacial modules by measurements and modelling, Energy Procedia 77 (2015) 364–373, [Online]. Available: https://www.sciencedirect.com/science/article/pii/S187661021500819X. 5th International Conference on Silicon Photovoltaics, SiliconPV 2015.

[55] J.A. Duffie, W.A. Beckman, Solar Energy Thermal Processes, third ed., John Wiley & Sons Inc, 2006.

[56] A. Smets, K. Jäger, O. Isabella, R. van Swaaij, M. Zeman, Solar Energy: The Physics and Engineering of Photovoltaic Conversion, Technologies and Systems, UIT Cambridge Limited, 2016.

[57] M.T. Patel, M.S. Ahmed, H. Imran, N.Z. Butt, M.R. Khan, M.A. Alam, Global analysis of next-generation utility-scale PV: Tracking bifacial solar farms, Appl. Energy 290 (2021) 116478, [Online]. Available: https://www.sciencedirect.com/science/article/pii/S0306261921000428.

[58] D. Berrian, J. Libal, M. Klenk, H. Nussbaumer, R. Kopecek, Performance of bifacial PV arrays with fixed tilt and horizontal single-axis tracking: Comparison of simulated and measured data, IEEE J. Photovolt. 9 (6) (2019) 1583–1589.

[59] C.D. Rodríguez-Gallegos, H. Liu, O. Gandhi, J.P. Singh, V. Krishnamurthy, A. Kumar, J.S. Stein, L. Li, S. Wang, T. Reindl, I.M. Peters, Techno-economic performance modelling of bifacial and tracking PV systems worldwide, in: 2021 IEEE 48th Photovoltaic Specialists Conference, PVSC, 2021, pp. 0406–0409.

[60] C.D. Rodríguez-Gallegos, O. Gandhi, S.K. Panda, T. Reindl, On the PV tracker performance: Tracking the sun versus tracking the best orientation, IEEE J. Photovolt. 10 (5) (2020) 1474–1480.

[61] X. Sun, M.R. Khan, C. Deline, M.A. Alam, Optimization and performance of bifacial solar modules: A global perspective, Appl. Energy 212 (2018) 1601–1610, [Online]. Available: https://www.sciencedirect.com/science/article/pii/S0306261917317567.

[62] E. Lorenzo, On the historical origins of bifacial PV modelling, Sol. Energy 218 (2021) 587–595, [Online]. Available: https://www.sciencedirect.com/science/article/pii/S0038092X21001869.

[63] M. Alam, M.S. Gul, T. Muneer, Ground view factor computation model for bifacial photovoltaic collector field: uniform and non-uniform surfaces, Energy Rep. 7 (2021) 9133–9149, [Online]. Available: https://www.sciencedirect.com/science/article/pii/S2352484721013457.

[64] M.T. Patel, M.R. Khan, X. Sun, M.A. Alam, A worldwide cost-based design and optimization of tilted bifacial solar farms, Appl. Energy 247 (2019) 467–479, [Online]. Available: https://www.sciencedirect.com/science/article/pii/S0306261919305604.

[65] M.T. Patel, R.A. Vijayan, R. Asadpour, M. Varadharajaperumal, M.R. Khan, M.A. Alam, Temperature-dependent energy gain of bifacial PV farms: A global perspective, Appl. Energy 276 (2020) 115405, [Online]. Available: https://www.sciencedirect.com/science/article/pii/S030626192030917X.

[66] D. Chudinzow, J. Haas, G. Díaz-Ferrán, S. Moreno-Leiva, L. Eltrop, Simulating the energy yield of a bifacial photovoltaic power plant, Sol. Energy 183 (2019) 812–822, [Online]. Available: https://www.sciencedirect.com/science/article/pii/S0038092X19302993.

[67] S. Guo, T.M. Walsh, M. Peters, Vertically mounted bifacial photovoltaic modules: A global analysis, Energy 61 (2013) 447–454, [Online]. Available: https://www.sciencedirect.com/science/article/pii/S0360544213007275.

[68] V. Durković, Ž. Durišić, Extended model for irradiation suitable for large bifacial PV power plants, Sol. Energy 191 (2019) 272–290, [Online]. Available: https://www.sciencedirect.com/science/article/pii/S0038092X19308448.

[69] W. Gu, T. Ma, M. Li, L. Shen, Y. Zhang, A coupled optical-electrical-thermal model of the bifacial photovoltaic module, Appl. Energy 258 (2020) 114075, [Online]. Available: https://www.sciencedirect.com/science/article/pii/S0306261919317623.

[70] Y. Zhang, J.Q. Gao, Y. Yu, Q. Shi, Z. Liu, Influence of incidence angle effects on the performance of bifacial photovoltaic modules considering rear-side reflection, Sol. Energy 245 (2022) 404–409, [Online]. Available: https://www.sciencedirect.com/science/article/pii/S0038092X22005771.

[71] M.R. Khan, E. Sakr, X. Sun, P. Bermel, M.A. Alam, Ground sculpting to enhance energy yield of vertical bifacial solar farms, Appl. Energy 241 (2019) 592–598, [Online]. Available: https://www.sciencedirect.com/science/article/pii/S0306261919301278.

[72] U.A. Yusufoglu, T.M. Pletzer, L.J. Koduvelikulathu, C. Comparotto, R. Kopecek, H. Kurz, Analysis of the annual performance of bifacial modules and optimization methods, IEEE J. Photovolt. 5 (1) (2015) 320–328.

[73] K.R. McIntosh, M.D. Abbott, G. Loomis, B.A. Sudbury, A. Mayer, C. Zak, J. Meydbrey, Irradiance on the upper and lower modules of a two-high bifacial tracking system, in: 2020 47th IEEE Photovoltaic Specialists Conference, PVSC, 2020, pp. 1916–1923.

[74] J.E. Castillo-Aguilella, P.S. Hauser, Multi-variable bifacial photovoltaic module test results and best-fit annual bifacial energy yield model, IEEE Access 4 (2016) 498–506.

[75] J.E. Castillo-Aguilella, P.S. Hauser, Bifacial photovoltaic module best-fit annual energy yield model with azimuthal correction, in: 2016 IEEE 43rd Photovoltaic Specialists Conference, PVSC, 2016, pp. 3109–3112.

[76] I. Shoukry, J. Libal, R. Kopecek, E. Wefringhaus, J. Werner, Modelling of bifacial gain for stand-alone and in-field installed bifacial PV modules, Energy Procedia 92 (2016) 600–608, [Online]. Available: https://www.sciencedirect.com/science/article/pii/S1876610216304520. Proceedings of the 6th International Conference on Crystalline Silicon Photovoltaics (SiliconPV 2016).

[77] A. Asgharzadeh, T. Lubenow, J. Sink, B. Marion, C. Deline, C. Hansen, J. Stein, F. Toor, Analysis of the impact of installation parameters and system size on bifacial gain and energy yield of PV systems, in: 2017 IEEE 44th Photovoltaic Specialist Conference, PVSC, 2017, pp. 3333–3338.

[78] U.A. Yusufoglu, T.H. Lee, T.M. Pletzer, A. Halm, L.J. Koduvelikulathu, C. Comparotto, R. Kopecek, H. Kurz, Simulation of energy production by bifacial modules with revision of ground reflection, Energy Procedia 55 (2014) 389–395, [Online]. Available: https://www.sciencedirect.com/science/article/pii/S1876610214013368. Proceedings of the 4th International Conference on Crystalline Silicon Photovoltaics (SiliconPV 2014).

[79] S. Wang, O. Wilkie, J. Lam, R. Steeman, W. Zhang, K.S. Khoo, S.C. Siong, H. Rostan, Bifacial photovoltaic systems energy yield modelling, Energy Procedia 77 (2015) 428–433, [Online]. Available: https://www.sciencedirect.com/science/article/pii/S1876610215008280. 5th International Conference on Silicon Photovoltaics, SiliconPV 2015.

[80] J. Appelbaum, Bifacial photovoltaic panels field, Renew. Energy 85 (2016) 338–343, [Online]. Available: https://www.sciencedirect.com/science/article/pii/S0960148115300732.

[81] C.W. Hansen, R. Gooding, N. Guay, D.M. Riley, J. Kallickal, D. Ellibee, A. Asgharzadeh, B. Marion, F. Toor, J.S. Stein, A detailed model of rear-side irradiance for bifacial PV modules, in: 2017 IEEE 44th Photovoltaic Specialist Conference, PVSC, 2017, pp. 1543–1548.

[82] M.R. Khan, A. Hanna, X. Sun, M.A. Alam, Vertical bifacial solar farms: Physics, design, and global optimization, Appl. Energy 206 (2017) 240–248, [Online]. Available: https://www.sciencedirect.com/science/article/pii/S0306261917310589.

[83] L. Kreinin, A. Karsenty, D. Grobgeld, N. Eisenberg, PV systems based on bifacial modules: Performance simulation vs. design factors, in: 2016 IEEE 43rd Photovoltaic Specialists Conference, PVSC, 2016, pp. 2688–2691.

[84] Z. Zengwei, Z. Zhen, J. Yongfeng, L. Haolin, Z. Shengcheng, Performance analysis on bifacial PV panels with inclined and horizontal east–west sun trackers, IEEE J. Photovolt. 9 (3) (2019) 636–642.
[85] M.T. Patel, M. Ryyan Khan, A. Alnuaimi, O. Albadwawwi, J.J. John, M.A. Alam, Implications of seasonal and spatial albedo variation on the energy output of bifacial solar farms: A global perspective, in: 2019 IEEE 46th Photovoltaic Specialists Conference, PVSC, 2019, pp. 2264–2267.
[86] D. Berrian, J. Libal, A comparison of ray tracing and view factor simulations of locally resolved rear irradiance with the experimental values, Prog. Photovolt., Res. Appl. 28 (6) (2020) 609–620, [Online]. Available: https://onlinelibrary.wiley.com/doi/abs/10.1002/pip.3261.
[87] M.A. Anoma, D. Jacob, B.C. Bourne, J.A. Scholl, D.M. Riley, C.W. Hansen, View factor model and validation for bifacial PV and diffuse shade on single-axis trackers, in: 2017 IEEE 44th Photovoltaic Specialist Conference, PVSC, 2017, pp. 1549–1554.
[88] P. Tillmann, K. Jäger, C. Becker, Minimising the levelised cost of electricity for bifacial solar panel arrays using Bayesian optimisation, Sustain. Energy Fuels 4 (2020) 254–264, [Online]. Available: http://dx.doi.org/10.1039/C9SE00750D.
[89] G. Janssen, R. Gali, K. de Groot, A. Carr, B. Van Aken, I. Romijn, Impact of inhomogeneous irradiance at the rear of bifacial panels on modelled energy yield, in: 33rd European PV Solar EnergyConference and Exhibition, EU PVSEC, 2018.
[90] R. Perez, R. Seals, P. Ineichen, R. Stewart, D. Menicucci, A new simplified version of the perez diffuse irradiance model for tilted surfaces, Sol. Energy 39 (3) (1987) 221–231, [Online]. Available: https://www.sciencedirect.com/science/article/pii/S0038092X87800312.
[91] N. Martin, J. Ruiz, Calculation of the PV modules angular losses under field conditions by means of an analytical model, Sol. Energy Mater. Sol. Cells 70 (1) (2001) 25–38, [Online]. Available: https://www.sciencedirect.com/science/article/pii/S0927024800004086.
[92] M.A. Green, Solar cells: operating principles, technology, and system applications, 1982, [Online]. Available: https://www.osti.gov/biblio/6051511.
[93] Meteonorm software, 2023, https://meteonorm.com/en/. Accessed on February 16, 2023.
[94] PVMD group, TU Delft, Database for global hourly irradiance spectra with 1° x1° resolution, 2023.
[95] D. Myers, C. Gueymard, Description and Availability of the Smarts Spectral Model for Photovoltaic Applications, Vol. 5520, 2004, pp. 56–67.
[96] J. Carolus, J.A. Tsanakas, A. van der Heide, E. Voroshazi, W. De Ceuninck, M. Daenen, Physics of potential-induced degradation in bifacial p-PERC solar cells, Sol. Energy Mater. Sol. Cells 200 (2019) 109950, [Online]. Available: https://www.sciencedirect.com/science/article/pii/S092702481930279X.